This is a preprint, the final version is subject to change, of the American Mineralogist (MSA)
Cite as Authors (Year) Title. American Mineralogist, in press.
(DOI will not work until issue is live.) DOI: http://dx.doi.org/10.2138/am-2017-5739

REVISION 1

Nuclear-blast induced nanotextures in quartz and zircon within Trinitite

Aaron J. Lussier[1], Sergei Rouvimov[2], Peter C. Burns[1,3] & Antonio Simonetti[1]

1. Department of Civil & Environmental Engineering & Earth Sciences, University of Notre Dame, Notre Dame, IN, 46556.
2. Department of Electrical Engineering, University of Notre Dame, Notre Dame, IN, 46556
3. Department of Chemistry and Biochemistry, University of Notre Dame, Notre Dame, In, USA, 46556.

ABSTRACT

The intense heat and pressure resulting from the detonation of the world's first nuclear device in the New Mexico desert, 16 July, 1945, severely altered the arkosic sand, producing the fused, glassy material referred to as Trinitite. The study of Trinitite is key to the development of nuclear forensic techniques that can provide crucial information about a nuclear event, such as device composition and radionuclide distribution. Moreover, nuclear blasts are often considered analogues to catastrophic natural events such as meteorite impacts, and it is well-documented that with increasing impact severity, zircon and quartz grains deform systematically. In Trinitite, a sufficient number of primary quartz and zircon grains remain identifiable. Here, a multi-technique approach (focused ion beam, scanning electron microscopy, aberration-corrected transmission electron microscopy, and micro-Raman spectroscopy) is employed to study the micron-to-nanometer-scale deformation features in altered grains of zircon and quartz in order to constrain blast pressure and temperature conditions. Trinitite zircon grains consistently show an outer halo of fibrous baddeleyite, radiating from a relatively unaltered core; HRTEM images show complex twinning, likely originating from an intermediate, tetragonal zirconia precursor. Trinitite quartz grains show various states of melting that appear to vary predictably with depth below the surface of the desert sand. Grains occurring deeper than ~1.5 cm are crystalline, with occasional planar fractures at the optical scale. At shallower depths, a systematic increase in quartz vitrification is observed. Considered together, these data suggest maximal temperatures in excess of 1500 °C and pressures of <10 GPa, the latter being considerably less than for any natural impact event. Taken in a broader context, the

42 implications of this work extend towards exploiting the use of advanced imaging
43 techniques to improve our understanding of mineral processes in extreme, non-
44 equilibrium environments at the near-atomic scale.

45

46 *Keywords:* Trinitite, zircon, martensitic twins, baddeleyite, focused-ion beam,
47 transmission electron microscopy, micro-Raman spectroscopy.

48

INTRODUCTION

The world's first nuclear detonation occurred at 05:29:45 on 16 July, 1945 at the White Sands Proving grounds, a remote patch of desert in New Mexico, USA. The plutonium implosion nuclear device referred to simply as "*The Gadget*" produced a blast equivalent to ~21 kt of TNT, and was of similar design to the "Fat Man" bomb dropped on the city of Nagasaki just several weeks later on 9 August. The blast resulted in intense heat and pressure that fused the mineralogically simple arkosic desert sand (Staritzky 1950) into the post-detonation material (PDM) now referred to as '*Trinitite*'. This complex material shows remarkable compositional and textural inhomogeneity from the hand sample to the nanometer scale (see Bellucci et al. 2014; Eby et al. 2015). Although the first detailed petrologic description of the Trinitite material dates back to Ross (1948), it has been little studied until the past decade. Growing interest in nuclear forensics research has resulted in increased focus on PDMs, since these may elucidate significant clues as to bomb design, fuel composition, and source and processing of fissile materials. In the aftermath of a nuclear event, this type of forensic information could be key to identifying the responsible party (or parties), and reconstructing an accurate chain of events that resulted in the incident. Trinitite is an ideal PDM on which to work, as many of these details are known (Parekh et al. 2006; Rhodes 1986). Previous investigations have shown the success of using textural (Bellucci and Simonetti 2012; Eby et al. 2015), compositional (Bellucci et al. 2014; Bellucci et al. 2013c; Donohue et al. 2015; Eby et al. 2015; Fahey et al. 2010; Koeman et al. 2013; Wallace et al. 2013) and isotopic (Bellucci et al. 2013a; Bellucci et al. 2013b; Koeman et al. 2013) information to corroborate many of the bomb details. It has also been

72 suggested that nuclear explosions may be analogous to natural, catastrophic events, in
73 that similar alteration features may be observed in the affected geological materials. For
74 instance, Eby et al. (2015) notes that Trinitite shares various characteristics with
75 fulgerites, which are produced as lightning strikes sand, and tektites, resulting from
76 meteorite impacts.

77 The shock alteration of zircon and quartz grains has been extensively studied in both
78 naturally (Chen et al. 2013; Grieve et al. 1996; Gucsik et al. 2004b; Joreau et al. 1996;
79 Nakano et al. 2008; Pidgeon et al. 2011; Schmieder et al. 2011; Trepmann 2008;
80 Trepmann and Spray 2006; Wittmann et al. 2006; Zanetti et al. 2014) and
81 experimentally (Gratz 1984; Grieve et al. 1996; Gucsik et al. 2004a; Kusaba et al. 1985;
82 Langenhorst 1994; Langenhorst and Deutsch 1994; Leroux et al. 1999; McMillan et al.
83 1992; Timms et al. 2014) shocked specimens. Cordier and Gratz (1995) also examined
84 quartz shocked by subsurface nuclear explosions at the Sedan test by TEM and found
85 extensive evidence of deformation in the form of crystallographically oriented plan
86 deformation features (PDFs). Such studies have repeatedly shown that deformational
87 (planar micro- fractures, crystallographic defects, granularization, and diaplectic
88 glasses) and phase transitional features arise systematically with increasing
89 temperatures and shock pressures. Observing the occurrence and distribution of such
90 features thus proves to be a highly useful petrological tool, from which information about
91 maximum pressure and thermal shock conditions, as well as thermal post-impact
92 histories can be derived.

93 Altered, primary quartz and zircon grains occur readily in Trinitite. Here we use a
94 combination of micro-Raman spectroscopy and various forms of microscopies (optical,

scanning electron, and aberration-corrected transmission electron) to investigate the external and internal textures in Trinitite quartz and zircon grains in order to constrain the pressure-temperature conditions resulting from the nuclear explosion.

METHODOLOGY

Trinitite material

A suite of samples of Trinitite material was acquired from the Mineralogical Research Company (www.minresco.com). Upon carefully selecting samples that showed disparate textural and mineralogical properties, a series of thick sections (~100 μm) were prepared; these have been used in multiple studies at the University of Notre Dame (Bellucci and Simonetti 2012; Bellucci et al. 2014; Bellucci et al. 2013a; Bellucci et al. 2013b; Bellucci et al. 2013c; Donohue et al. 2015; Koeman et al. 2013; Wallace et al. 2013), and consistent sample nomenclature is used here.

In Trinitite, two texturally distinct zones are commonly observed. The '*glassy side*' extends to depths of ~1-2 cm from the post-detonation desert surface. Relic grains of quartz and feldspar, and less commonly zircon and apatite, are found embedded in the glassy matrix. This region also shows the highest concentrations of bomb-derived elements such as U, Pu, Pb, and Cu (Bellucci et al. 2013b; Donohue et al. 2015; Wallace et al. 2013). The '*sandy side*' occurs at depths greater than ~2 cm and consists mostly of mineral grains showing lesser degrees of alteration and coarser textures. In this region, nearly insignificant concentrations of bomb-derived alpha-particle-emitting nuclides are found. For this study, as with that of Donohue et al. (2015), care was taken

to select sections cut with a clear vertical orientation, such that both glassy and sandy regions were readily identifiable.

Grain selection

Both quartz and zircon grains were initially located in thin section by conventional optical microscopy and confirmed using an EDAX Orbis micro-XRF, which mapped the [2]-dimensional distribution of Si (Kα line) and Zr (Kα line) over the extent of several thin sections. The maximal resolution of the Orbis system is ~30 um, allowing easy detection of quartz grains, which are typically >100 um in width (Figure 1). The small diameters of zircon grains (typically <50 um) required further confirmation using a LEO (EVO-50) scanning electron microscope, operating (mostly) in backscatter electron mode and equipped with X-ray fluorescence detection. Sections were sputtered with Ir^{+} to improve image quality. A selection of zircon and quartz grains, occurring in both the glass and sandy regions are imaged in Figures 1 and 7.

Focused-ion beam and transmission electron microscopy

A single zircon grain from glassy section of TS1 (referred to as Zr09), showing very distinct halo and core textures (Figure 1g) was chosen for further study by FIB and TEM. A FEI Helios 600 Dual-beam Focused Ion Beam (FIB) was used to extract the TEM foil. The location of the foil (dotted blue line, Figure 1g) was carefully chosen, such that it would contain sufficient amounts of core and fibrous materials. The excavated trench feature sputtered during the foil extraction procedure is shown in Figure 1h. In

addition, TEM foils from a representative selection of quartz grains were also prepared by FIB.

Foils were extracted, thinned, and polished to <100 nm using a Ga^+ beam operating between 30 and 1 keV. The prepared foil was then mounted on Cu holder and examined using a FEI Titan transmission electron microscope (TEM) operating at either 80 keV (quartz) or 300 keV (zircon). All images were processed after acquisition using the Gatan Microscopy Suite (www.gatan.com). To acquire high-resolution compositional data, the instrument was set to operate in scanning-transmission (STEM) mode and data were acquired along linear traverses using the INCA EDX system (Oxford Instruments Inc.).

Micro-Raman Spectroscopy

An NRS-5100 Jasco μ-Raman spectrometer with a 50 mW 532 nm (green) laser, equipped with a Peltier-cooled CCD detector, was used to collect spectra on selected quartz and zircon grains over the ranges of 90 to 1800 cm^{-1}. A 100X optical objective was used to focus the laser on the sample surface and the instrument was set to operate in quasi-backscattering mode with ~2 mW of laser power interacting with the sample surface. Repeated analysis on the same location showed no degradation of spectral quality, suggesting no sample damage occurred due to laser adsorption. The system focal length is 300 mm. The system aperture was set to 20 μm (for both spot analysis and 2-dimensional mapping) and the final spectral resolution was 7.02 cm^{-1} (1.83 cm^{-1}/pixel). Prior to all analyses, the system was calibrated to a pure Si standard (520.9 cm^{-1} band). All samples were optically polished and cleaned immediately prior to

data collection. Each spectrum is the average of three scans, totaling approximately one minute of integration time. Several zircon and quartz grains were subjected to detailed Raman analysis; however only spectra from representative zircon samples are shown below, and spectra from quartz are not illustrated as no useful deviation from characteristic reference spectra are displayed (*e.g.*, RRUFF-R040031; Downs 2006).

RESULTS

Trinitite zircons

A selection of 20 Trinitite zircon grains were located throughout the glassy and sandy regions and imaged (secondary electrons); a representative selection of these is shown in Figure 1. Grains are generally equant, with diameters ranging from 15 to >100 μm (average 50 μm). Zircon grains typically consist of a central, massive region with no apparent deformation or fractures. The central region is mantled by fibrous material that radiates in an outward direction for distances of ~5-15 um. Although they occur in very close proximity, no clear physical contact between the core and fibers is observed. Some zircons are characterized by a fibrous texture material extending throughout the entire grain (Figure 1f). The outline of some grains (Figure 1a,b,e) appear planar with angled edges possibly consistent with the primary crystal faces, whereas others show highly irregular (Figure 1h) or rounded (Figure 1d,f) edges. Each zircon grain was examined carefully using SEM backscattered electron (BSE) imaging for the presence of any primary compositional zoning features; none were detected. The grain imaged in Figure 1d appears to show evidence of brittle fracture behavior, whereas the grain in Figure 1*c* shows little evidence of fibrous alteration product; here, the close proximity of

the individual grains suggests they originate from a common fractured precursor grain. Figure 1e shows an SEM-BSE image of the grain selected for further study by TEM.

Raman spectroscopy of zircon: A total of 5 zircon grains were examined by micro-Raman spectroscopy. Typical Raman spectra observed for both the core and fibrous regions are shown in Figure 2 (*Zr** indicates the locations of characteristic zircon bands). In the spectra from the core region, three characteristic (see RRUFF dabase-R10018; Downs 2006) zircon bands at ~1009, ~437, and ~357 cm^{-1} are prominently visible, whereas characteristic bands at ~975 and 198-225 cm^{-1} are present with very low less intensity (Figure 2a). Each of these bands is notably absent in the spectrum from the fibrous region (Figure 2b). In the Raman spectra corresponding to both core and fibrous regions, bands between 400 and 600 cm^{-1} are present that clearly do not correspond to zircon (Figure 2a, b). Variation in the intensity of the Raman bands centered at 590 cm^{-1} and 1006 cm^{-1} across the traverse indicated in Figure 1a are illustrated in Figures 2c and 2d. The band at 590 cm^{-1} is relatively strong in the fibrous material and essentially absent in core. Conversely, the intensity of the characteristic zircon band (at 1006 cm^{-1}) is consistently high in the zircon core and absent in the fibrous material.

During a natural impact event, zircons may undergo a series of phase transformations. At shock pressure exceeding 20 GPa, reidite, the high pressure $ZrSiO_4$ polymorph is typically present (Chen et al. 2013; Glass et al. 2002; Gucsik et al. 2004b; Turner et al. 2014). At temperatures exceeding 1700 °C, the decomposition of zircon to crystalline ZrO_2 (usually tetragonal) and amorphous SiO_2 occurs. Although there are at

208 least six known ZrO_2 polymorphs, the ZrO_2 phase typically corresponds to the mineral
209 baddeleyite (monoclinic ZrO_2) when observed under ambient conditions, or small
210 volumes of the relict tetragonal phase. In natural samples, altered zircon grains may
211 occur with a fibrous halo of baddeleyite that mantles a core of primary zircon material
212 (Chen et al. 2003; Wittmann et al. 2006), similar to the textures observed here in
213 Trinitite.

214 Comparison of the observed spectra to those of either reidite (Knittle and Williams
215 1993) or baddeleyite (Figure 2f) does not yield an obvious match. For completeness,
216 the spectra were also compared to those of other ZrO_2 [tetragonal, del Monte 2000;
217 isometric, RRUFF-R04142 Downs 2006; orthorhombic-I, Ravindran and Yadav 2015;
218 cotunnite-type, Haines et al. 1997] and SiO_2 [tridymite, stishovite, cristobalite, coesite;
219 RRUFF database; Downs 2006]; no conclusive match was observed. As presented in
220 greater detail below, energy-dispersive spectroscopy (Figure 4) and high-resolution
221 TEM (HRTEM) / selected area electron diffraction (SAED) images collected on the
222 fibrous material are shown in Figures 5-6 and (as discussed below) indicate a chemical
223 composition and a unit cell, respectively, that are consistent only with the fibrous
224 material being monoclinic ZrO_2 (baddeleyite), albeit with a volume reduced by ~9% from
225 typically-observed values for specimens listed in Inorganic Crystal Structure Database
226 (2015). Reasons for the inconsistent nature of the Raman analysis cannot be resolved
227 with the current dataset; however anomalous bands resulting from photoluminescence
228 due to the presence of trace REEs (Lenz et al. 2015), or band shifting due to phonon
229 confinement (observed in other systems with nano-crystals (Bersani et al. 1998;

Gouadec and Colomban 2007) and nano-twinning (Arora et al. 2007; Kumar et al. 2012), and the presence multiple phases are possibilities worthy of future investigation.

Zircon nanoscale petrography

A low magnification TEM image of the prepared zircon foil is shown in Figure 3a, and the colored boxes correspond to regions shown at higher magnification in Figures 3b-g. The central region appears as massive, continuous material in the lower right portion of the image. A diffraction pattern (inset lower right in Figure 3a), corresponding to zone axis [111] confirms this phase to be zircon and an HRTEM image taken from the bulk material (Figure 3b) shows no obvious deformation features, such as planar fractures or crystallographic defects. No diffraction was observed corresponding to the interstitial material (light gray in Figure 3a, c, d), confirming it to be amorphous. The variation in elemental abundances of Si, Zr, and O along the traverse section shown in Figure 4a is plotted in Figure 4b. In agreement with the phase identification by Raman spectra, the zircon core and baddeleyite fibers consists of ZrO_2-SiO_2 and of ZrO_2, respectively; however, the interstitial glass consists solely of SiO_2, and no other elements were detected.

The baddeleyite fibers occur either as elongated structures, ranging in width from 0.2 to 0.4 μm and in (apparent) length from ~0.8 to 7 μm. Several appear as circular structures, likely owing to the cross-cutting orientation of the TEM foil. The long axes of the elongated fibers are consistently oriented perpendicular to the zircon-glass interface. Images shown at higher magnifications (Figures 3c-g) reveal that nearly every fiber shows prominent, parallel lamellar features that cross-cut the fibers at almost

perpendicular angles to the long axis. These features are typically (Figure 3d, g), yet not always (Figure 3d) continuous across the entire width of the fiber. For clarity, the TEM image shown in Figure 3*a* is reproduced as a trace in Figure 3h. Here, the green dotted lines indicate the average direction of the fiber axes. Two orientations of lamellae are observed, corresponding to the dotted purple and orange lines. The sub-parallel alignment of each line color highlights the consistent orientation of lamellae across multiple, physically separated and differently-oriented fibers. The majority of fibers show a lamellar orientation corresponding to the purple line, whereas only a small number show an orientation corresponding to the orange lines in (Figure 3h).

Throughout the sample, the zircon/glass and baddeleyite/glass boundaries appear sharp on the sub-micron scale, and no well-formed crystallographic faces are observed. No fibers directly contact the central, core region; amorphous material is always present to separate the two phases. In one region, (green box in Figure 3a ,g) a fiber cross-section appears to be pinched from the bulk core. This is the only instance in which there appears to be a clear, interaction between a fiber and the bulk zircon, although amorphous material still clearly separates the two structures. The higher-magnification image shown in Figure 3e (blue box) shows the lamellar features correspond to twin planes that distinguish nanometer-scale twins of baddeleyite. The individual twins are typically between 20-30 nm in width and are in nearly perfect, parallel alignment.

Nanoscale twins in baddeleyite fibers

A partial image of a fiber cross section (blue arrow in Figure 3a), constructed of adjacent TEM micrographs, (Fiber 5; blue arrow in Figure 3a) is shown in Figure 5b.

The grain shows parallel twin planes that are continuous across the diameter; dashed blue lines highlight these planes. The HRTEM images (Figure 5c-d) very clearly show the twin planes and the corresponding differences in lattice orientations. The colored arrows (pink, purple, green; Figure 5c-d) are aligned with the lattices; they, as well as the distinctly-colored backgrounds in Figure 5b, highlight the three different twin variants observed in the fiber.

Figure 6a shows a SAED image taken from the central part of the grain (*i.e.*, a region showing all three twins). Diffraction patterns, calculated from Fourier transforms of HRTEM images of each twin variant, show the three patterns illustrated in Figure 6b-d (note: the colors of the borders coincide with the colors of the double-headed arrows in Figure 5). The oblique net shown in Figures 6a and 6b both correspond to the monoclinic, baddeleyite cell, imaged with electron beam down [010] (pink variant) and [0-10] (green variant) respectively. The rectangular lattice (Figure 6c) also corresponds to the baddeleyite cell, imaged with the electron beam oriented down either [100] or [-100], which both correspond to indistinguishable diffraction patters (purple variant). Superposition of these three calculated diffraction patterns (each to correct scale) is shown schematically in Figure 6e, and the indexed patterns are presented in Figure 6f. The complex, symmetric pattern of diffraction spots observed in Figure 6a is recreated accurately only when the axial vectors of the three twin variants are aligned in the relative orientations indicated in Figure 6g.

The distribution of the three twin variants in Figures 5a-d shows three types of adjacencies. As indicated by the double-headed colored arrows, orange-green, purple-green, and purple-purple are observed; the purple-orange adjacency is not observed (at

299 least not in this grain). Thus, three crystallographic orientation twin relationships can be
300 established:
301 (1) [100] // [100]; [010] // [0-10] and (010) // (010) (red-blue)
302 (2) [100] // [100]; and (010) // (100) (blue-green)
303 (3) [100] // [-100] and (001) // (00-1) (green-green).
304 The latter twin relationship occurs because the space group $P2_1/c$ lacks a mirror
305 plane oriented along (100). The crystal structures of baddeleyite, when projected down
306 [100] and [-100], are enantiomeric; however, the resulting electron diffraction patterns
307 are superimposable.
308 The orientational relationship between the core zircon and fibrous baddeleyite
309 material was examined by closely comparing the SAED patterns. The orientation of a
310 zircon zone axis orientation was found using the double-tilt TEM holder. Without altering
311 the holder orientation, diffraction patterns corresponding to multiple fibers were taken for
312 comparison. This was done for several zircon zone axis. Crystallographic orientations of
313 both zircon and baddeleyite were plotted in a stereonet to clearly establish orientational
314 relationship. Shifting and rotation of the fibrous baddeleyite material, on the order or 10-
315 15°, obscured the absolute relationship to the core zircon. However, it could be
316 established with reasonable certainty that, with respect to the baddeleyite twin variant
317 highlighted in red (Figure 6), $(001)_{bd}$ was observed to contain both $[111]_{zr}$ and $[001]_{zr}$.
318 This suggests $(001)_{bd}$ to be subparallel with $(1\text{-}10)_{zr}$. As the (001) planes of all
319 baddeleyite twin variants illustrated in Figures 6 and7 exist in parallel orientation (Figure
320 6g), this relation holds true for each twin. This result strongly suggests a non-random
321 orientational relationship between the primary zircon and the fibers.

From the twinned diffraction image, the cell parameters for Trinitite baddeleyite can be estimated. For each parameter, 10 individual measurements were averaged, arriving at *a*, 4.91(1), *b*, 4.97(1), *c*, 5.27(6) and *β*, 99.5(5)°, respectively. The average of 49 reported cell diameters from the ICSD is *a*, 5.15(3) Å, *b*, 5.20(3) Å, *c*, 5.32(3) Å, and β, 99.2(3)°. Despite the relatively good agreement between these cells, the data suggest a ~9% reduction in volume compared to the average baddeleyite cell; this effect is particularly significant with respect to the *a* and *b* lattice parameters.

Trinitite quartz

The regions of elevated silica (devoid of any other element) in the Trinitite thin sections indicated by XRF are initially assumed to correspond to quartz (or potentially another silica polymorph). Investigation of these regions by optical microscope, however, reveals the occurrence of three distinct types of grains.

Type-I quartz: These quartz grains show a characteristic, relatively sharp extinction with typical, first order birefringence and pronounced relief, relative to the surrounding matrix of Trinitite glass. These grains range from anhedral to subhedral and from <50 – 200 μm in size. Physical deformation is frequently observed in type-I grains, either as cracks of irregular orientation (*e.g.*, blue arrows, Figure 7a-d) or (less commonly) sets of parallel, planar deformation fractures (red arrow, Figure 7c-d) with a preferred orientation. Quartz grains of this type dominate the sandy areas of Trinitite sections, and are also (very rarely) observed in the glass regions (see Figure 10a)

Type-II quartz: These grains are predominantly anhedral and range in size from 100-200 μm. In plane-polarized light (Figure 7e, h), these quartz grains show a dark, mottled core with medium relief, often surrounded by a clear, colorless rim of low optical relief. In cross-polarized light (Figure 7f, h), the interiors shows discontinuous regions of mottled birefringence, however these regions show a consistent extinction angle and thus implied crystallographic continuity. Cracks of irregular orientation are often observed throughout these grains but are mostly located towards the interiors. The Becke line shows a weak difference in refractive index between this grain border and the surrounding vitrified bulk Trinitite, suggestive of partial melting. The quartz grains consistently show a highly irregular shape with edges that are significantly rounded and devoid of any obvious primary faceting. Evidence of irregular fractures are consistently observed through these grains. Grains of this type are relatively rare, corresponding to <10% of the observed quartz grains.

Detailed imaging of the type-II quartz (form Trinitite section 5a 886b) is shown in Figure 8. Here, we can see extensive vitrification in the outer region as well as the persistence of fractures of irregular orientation through the grain. Bubbles (Figure 8b) are also present, concentrated towards the core boundary. In cross-polarized light (Figure 8c), only the lower left region shows clear birigfringence. Detailed investigation of these grains by Raman spectroscopy shows only spectra consistent with *α*-quartz (spectra not shown). The clear presence of small (<10 μm) fragments of crystalline material set in a glassy matrix is observed in an SEM image of the same area (Figure 8d).

Type-III quartz: The grains range in diameter from <10 to >200 μm and are highly irregular in shape, show no evidence of primary crystal faces and are mostly devoid of any fractures or other optical-scale deformation features. In plane-polarized light (Figure 7i), this type of grain is clear and colorless. In contrast with type-II grains, the entire grain is of very low relief. In cross-polarized light (Figure 7j), the grains appear completely isotropic with no visible extinction, indicating a lack of crystallinity. Rarely the remnants of crystalline cores are visible in the center of the grain (*e.g.*, red arrow, Figure 8a). The Becke line shows refractive indices to be nearly indistinguishable from that for the bulk Trinitite material. These grains are located exclusively in the glassy regions.

An example of the contact (dashed blue line) between the glassy (top) and sandy (bottom) regions is shown in Figure 7k, l. This image clearly shows that type-I grains are abundantly present only on the sandy side.

Raman spectra of quartz: In excess of a dozen quartz grains (type-I, -II, and –III) were studied in detail by Raman spectroscopy. Spectra were carefully examined for indications of (1) peak broadening and/or shifting resulting from exposure to shock pressure (McMillan et al. 1992), and (2) the presence of higher temperature (tridymite/cristobalite) and pressure (stishovite/coesite) polymorphs; none were observed. A series of high-resolution Raman traverses (step size <5 um) extending from grain interiors to edges of both types-I and –II quartz consistently yield spectra of only *α*-quartz (Figure 8d). Further, peak broadening/shift, relative to other published spectra of

pressure-shocked quartz was not observed. Type-III grains, as well as the outer (rim) regions of type-II grains, yield Raman spectra with no discernable bands (spectra not shown).

Quartz TEM imaging

Representative type-II and type-III quartz grains were selected for further study by TEM. The dotted red lines Figure 7 show the locations and orientations of the TEM foils extracted by FIB and imaged in Figure 9. Two examples of type-II quartz are shown, corresponding to Trinitite sections TS1 (Figure 9a-b) and 5a 886b (Figure 9c-d). The TEM images of the grain from TS1 show a highly complex deformation pattern, with non-linear veins of amorphous silica cross-cutting the grain. The crystalline area has many defects including grain boundaries and small inclusions with black-and-white contrast. There are many bending contours (dark lines) within the crystalline grains indicating the presence of residual internal strain. Micro-inclusions, as well as other deformational features are observed may indicate phase transformation that occurs at high temperature under high pressure conditions. The TEM image of the grain from section 5a 886b shows that the majority of the grain volume is amorphous silica (as evidenced by electron diffraction patterns). Small (0.2 – 1 um), highly irregular fragments of the crystalline *α*-quartz material occurs as islands surrounded by glass, consistent with the Raman and SEM images shown in Figure 8. In both bright field (Figure 9c) and dark field (Figure 9d) images, the remnant crystalline fragment shows bending contours (dark lines) that likely corresponding to residual internal strain, and small inclusions with black-and-white contrast due to strain around them although no

obvious brittle fractures are apparent. Note that the orientation of the stress lines appears to be continuous across multiple quartz islands.

In addition, two examples of type-I quartz grains from section 5b 10.22a are shown in (Figure 9e – red arrow Figure 7c-d) and (Figure 9f - blue arrow Figure 7c-d). In agreement with optical and Raman data, both of these grains lack any features associated with vitrification. Although both of these grains show evidence of fracture deformation under optical microscopy, features known to be related to the effects of very low grade pressure shock (see below), the corresponding TEM images, however, show only minor physical defects. Hence, the fractures are not obviously related to the internal grain structure. This counterintuitive discrepancy has been noted elsewhere in the literature (Stoffler and Langenhorst 1994). These grains do, however, show shadows in bright field images suggestive of lattice strain.

DISCUSSION

The origins of Trinitite constituents

Previous investigations (Bellucci et al. 2014; Donohue et al. 2015; Wallace et al. 2013) have shown that bomb-sourced radionuclides (*i.e.*, U and Pu) are well-mixed into the vitrified material that dominates the glassy upper ~2 cm of many Trinitite samples (Fig. 10). The distribution of these elements can result from two processes, (1) the introduction of radionuclides into freshly melted desert material by the initial blast and subsequent mixing by the passing shock wave, or (2) the redeposition of melted, contaminated fallout materials. The latter process results from the ability of afterwinds (wherein cool ambient air turbulently mixes with the hot air resulting from the explosion)

437 to carry large amounts of debris from the desert floor into the ascending fireball and
438 mushroom cloud. The amount of debris drawn up into the mushroom cloud is
439 approximately 0.1 Mt/Mt (Aherne et al. 2005) corresponding to ~2.1 Mt in the case of
440 the Trinity device, and hence can contribute significantly to the amount of altered
441 material observed on the desert floor. If the temperature of the hot air mass is sufficient
442 to melt the introduced material, radioactive contaminants may become incorporated into
443 the molten material. As the material coalesces, it is redeposited in a largely molten state
444 in the first wave of nuclear fallout, a radioactive silicate-rich 'rain'. The textural and
445 compositional complexity of Trinitite makes distinguishing between fallout and *in situ*
446 processes extremely difficult, however almost certainly both did occur. This clearly
447 complicates our ability to interpret the history of quartz and zircon grains distributed
448 throughout the Trinitite sections. Individual mineral grains, although located very close
449 to each other in the solidified PDM, may have experienced the blast (and immediate
450 aftermath) in fundamentally divergent ways. Differentiating these processes is further
451 complicated by the lack of precise data showing the distance individual specimens were
452 sampled from the blast site. Also, it is unclear if quartz and zircon have recorded the
453 thermal conditions experienced in the fireball/mushroom cloud, or those experienced by
454 the desert floor. These issues are considered and discussed in greater detail below.
455
456 *Zircon decomposition: temperature constraints*
457 The SEM and TEM images reported in this study clearly show the decomposition of
458 zircon into baddeleyite (*m*-ZrO_2) and silicate glass. Ambiguity persists in the literature
459 pertaining to the temperature of thermal decomposition of zircon. Under ambient

460 pressure conditions, the zircon decomposition temperature has been shown to vary as a
461 function of crystal size, purity, and heating time (Kaiser et al. 2008). Experimental
462 studies indicate (Anseau et al. 1976; Curtis and Sowman 1953; Kaiser et al. 2008;
463 Pavlik et al. 2001) that, with increasing temperature, the thermal decomposition (T_d) of
464 zircon occurs in two stages; decomposition begins at lower temperatures (1200 - 1600
465 °C) but with sluggish kinetics, and at T_d (1550-1675 °C), the decomposition rate
466 increases by several orders. However, even with small amounts of impurity, the value of
467 T_d may decrease significantly, largely resulting from the fact that in the ZrO_2-SiO_2
468 system, the eutectic and thermal decomposition temperatures differ only by ~15 °C, and
469 impurities dramatically affect the eutectic composition.
470 With increasing temperatures, pure *α*-quartz undergoes a series of phase
471 transformations to *β*-quartz (~580 °C), tridymite (~750 °C), cristobalite (~1490 °C), and
472 melt (~1750 °C) respectively. However, using this system to constrain the temperature
473 is complicated as (1) neither Raman nor TEM data indicate the presence of higher
474 temperature phases, despite the fact that these temperatures were clearly attained and
475 (2) the production of diaplectic silicate glass has been observed to occur at even very
476 low shock pressure (2.5 Gpa: Kowitz et al. 2013a). Thus, the heating rate was rapid
477 enough to result in the direct transition of α-quartz to glass at a temperature
478 significantly, <1750 °C required for vitrification in thermodynamic equilibrium. After the
479 blast, the materials apparently cooled sufficiently rapidly that no other phase could form.
480 Also, the pressure shock wave may further affect the vitrification temperature in
481 unpredictable ways. Further, we may speculate that the delicate textures of the

zircon/baddeleyite grains are more likely to have been preserved in those grains subjected to elevated temperatures while *in situ*.

The consistent orientational relationship between core zircon and fibrous baddeleyite material (as well as the orientational consistency observed with the baddeleyite fibres) material strongly suggests that the zircon material was altered to ZrO_2 (likely tetragonal at high temperatures – see below) without ever being detached from the primary zircon grain. This further suggests that alteration likely initiated at the grain/matrix boundary, progressing towards the grain interior.

Shock alteration of zircon and quartz: pressure constraints

Stoffler (1971) initially proposed that the intensity of thermal and pressure shock related to natural impact events corresponded to five (with a possible sixth) distinct stages, based largely on the Hugoniot-type behavior of framework silicates (*i.e.*, quartz and feldspar) in non-porous crystalline rocks. In a Hugoniot-type curve, the Hugoniot Elastic Limit (HEL) corresponds to the minimum shock pressure required to induce plastic deformation. Subsequently, other work has investigated the impact-related physical deformations and phase transitions in rock-forming minerals such as quartz (Cordier and Gratz 1995; Goltrant et al. 1991), zircon (Chen et al. 2013; Leroux et al. 1999; Piazolo et al. 2012; Pidgeon et al. 2011; Reimold et al. 2002; Wittmann et al. 2006; Zanetti et al. 2014), and, to a lesser extent, feldspar (Cygan et al. 1992; Huffman et al. 1993; Johnson et al. 2003; Lambert 1979; Ostertag 1983).

A predictable, systematic deformation of mineral grains is observed with increasing shock pressures and associated temperatures. A generalized, graphical representation

of these shock stages as they pertain to meteorite impacts is shown in Figure 11. The black curve shows the average conditions experienced during a meteorite impact. The five shock stages, as explained above, are shown in roman numerals on the right hand side of the diagram. The encircled numbers on this figure indicate key points for both zircon and quartz deformation. At point (0), no deformational features are observed in zircon grains, but planar fractures at the mm-scale are present in quartz grains. At point (1), planar micro-structures are observed in both quartz and zircon. Mosaicism (a highly mottled extinction texture) is commonly observed in quartz grains. Phase transitions to reidite and stishovite are also observed. At (2), the development of diaplectic glass and coesite from quartz is prevalent, whereas in zircon, granular textures, and decorated planar microstructures are visible. At (3), decomposition to ZrO_2 and amorphous SiO_2 occurs, and granular texture dominates the remaining zircon cores.

As mentioned above, some grains of type-I quartz show either random or planar fractures while the majority do not. Figure 11 indicates that such planar fractures to be the first deformational feature to be observed with increasing shock conditions. Other than these features, neither quartz nor zircon grains in Trinitite demonstrate evidence of physical deformational features, suggesting the HEL has not been greatly surpassed for either phase.

In porous materials, the collapsing of void spaces absorbs a significant amount of the incident shock energy. In a detailed TEM study of naturally shocked samples form the Coconino Sandstone from Meteor Crater, Arizona, moderate shocking ($10 < P < 25$ GPa) resulted in up to 50% of residual quartz grains showing fractures similar to those observed in type-I Trinitite grains, but otherwise no deformation was noted. In these

natural samples, however, quartz exists in direct contact with 18-32 wt% coesite and traces of stishovite at grain boundaries. Kowitz et al. (2013) demonstrated experimentally that in natural, porous Seeberger Sandstone subjected to low shock pressures ranging between 2.5 and 17.5 GPa, complete pore collapse and the initiation of diaplectic glass/silica melt development occurs. This is in marked contrast to the 30-35 and ~45 GPa required to induce diaplectic glass and silica melt, respectively, in single crystals of quartz (Kowitz et al. 2013b; Stoffler and Langenhorst 1994). Interestingly, (Kowitz et al. 2013a) report (their Figure 3) the development of textures in quartz grains found in porous sandstones shocked to 17.5 GPa at ambient temperatures that are remarkably similar to those illustrated in Figure 8d. These authors also state that they did not observe any stishovite/coesite production and concluded this to be due to differences in experimental *vs.* natural pressure pulse duration and post-shock temperatures. Further, systematic changes in band position (and FWHM for quartz) are observed in the Raman spectra of both zircon (Gucsik et al. 2004a) and *α*-quartz (McMillan et al. 1992) as pressures exceed 20 and 30 GPa, respectively. No such shifts are observed in any of the spectra collected on Trinitite specimens.

Distribution of quartz grains types

From the above images and discussion, it seems clear that quartz grains can be placed within a continuum of increasing thermal alteration, *i.e.*, type-I > type-II > type-III, since it is evidenced that vitrification increases, systematically from the outer edge to the inner core. The unaltered type-I quartz grains dominate the sandy regions of the Trinitite sections, and thus tend to occur in approximately their original locations in the

551 depth profile. These grains would have experienced the shock pressure required to
552 induce the observed, pervasive fracturing, but not the elevated temperatures required to
553 induce melting. The partially and completely vitrified type-II and type-III quartz grains,
554 respectively, thus correspond to material exposed to significantly higher temperatures.
555 The persistence of type-III amorphous SiO_2 grains in the glassy Trinitite is somewhat
556 contradictory. It is of interest that these grains remain discrete silicate entities, whereas
557 the surrounding silicate material exhibits thorough melting and mixing.
558 One possibility is that a short time (seconds time frame) after the initial blast, the
559 mushroom cloud temperature would decrease such that entrained desert materials
560 remain somewhat intact with less melting. These grains, subsequently redeposited as
561 fallout into the cooling, yet still molten, silicate matrix on the desert floor. Most
562 redeposited quartz grains would have been completely melted (evidenced by the
563 abundance of type-III grains), whereas some would have been only partially melted
564 (evidenced by the rarity of type-II grains). The extent of observed vitrification in these
565 grains is thus related to both (1) the temperature of mushroom cloud, (2) the
566 temperature (and cooling rate) of the molten desert floor, and (3) the initial size of the
567 grain.
568 This interpretation agrees with the observed distribution of quartz types in the
569 sections shown in Figure 10. For the sections TS1, 4F 5.37a, 5a 8.86b, and 4C856b,
570 the distributions of the three quartz types are shown in the images of the left column,
571 whereas the alpha-track radiographs for the corresponding sections are illustrated in the
572 images of the right column. The purple arrow indicates the vertical orientation (desert
573 floor on top) of each of the four sections, as determined by the distribution of both

alpha-tracks and coarser-grained/glassy material. Comparison of these images shows that the unaltered type-I quartz grains (highlighted in orange) predominantly occur in the coarse-grained 'sandy' material; type-II (green) and type-III (purple) quartz grains, however, are distributed through the glassy portion. The relatively rare occurrence of type-I grains in the glassy region, likely correspond to later stage fallout, as the mushroom cloud and the desert surface cooled to temperatures insufficient to induce melting.

Martinsitic phase transformations in the ZrO_2 system

At the temperatures required for zircon decomposition (>1500 °C), tetragonal ZrO_2 (*t*-ZrO_2) is the stable zirconia phase (see Figure 11). Neither TEM images nor Raman spectra show evidence for the presence of *t*-ZrO_2 in either the cores or the associated fibers of Trinitite zircon grains. During cooling over the temperature range of 950 to 1150°C, a martensitic (see Lee and Rainforth, 1994, and references therein) phase transformation between *t*- and *m*- zirconia is well-documented. Simply stated, a martensitic phase transformation results in an overall shape change, and a *habit plane*, common to both parent and product phases, remains unchanged by the transition. Muddle et al. (1986) determined this plane to correspond to (130). Additionally, in the *t* > *m* zirconia transition, a 5% increase in volume occurs.

The lack of any evidence indicating the presence of residual *t*-ZrO_2 suggests that the tetragonal phase either (1) did not crystallize at elevated temperature, or (2) has undergone a complete phase transformation to baddeleyite. Three lines of evidence support the occurrence of the latter. First, the TEM images of fibers reported here bear

a high degree of visual similarity to those previously reported, examining experimentally induced *t* > *m* transitions (Hannink et al. 2000; Hugo and Muddle 1993; Hugo et al. 1988; Muddle and Hannink 1986). Second, the zircon >> *t*-ZrO_2 >> *m*-ZrO_2 pathway has been demonstrated experimentally where zircon starting material has been heated to >1450 °C and cooled to ambient temperatures (Kaiser et al. 2008) with the reaction monitored by *in situ* powder X-ray diffraction. The estimates of the *t* > *m* transition temperatures are less than those at which the zircon decomposition occurred. Third, the development of baddeleyite twins, similar in scale to those observed here, has been proposed by Bail (1964) to be of deformational origin, resulting from the effective stress induced by the volume increase associated with the *t* > *m* martensitic transition in a constrained environment. Such stress also tends to result in the formation of microcracks, as observed along the twin planes in the HRTEM image (white arrow, Figure 5c). The latter point suggests that as the material cooled, the Trinitite matrix was in, at least, a semi-solid state prior to the onset of the *t* > *m* transition.

The orientation continuity observed between the individual baddeleyite fibers was clearly illustrated in Figure 3. This suggests that the orientations of the original *t*-ZrO_2 fibers were also in crystallographic continuity. Preference in crystallographic orientation often results from the application of a directional stress within the growth medium during crystallization, promoting the growth and alignment of a certain {*hkl*} form. This process is unlikely to have occurred here, as crystallographic continuity is maintained even though the orientation of different fibers changes considerably.

620 *Sequence of events*

621 The changes in pressure and temperature conditions associated with the detonation
622 of a nuclear device are so rapid that establishing a sequence of events in Trinitite
623 formation is a nontrivial endeavor. The petrographic evidence presented here allows the
624 inference of some details of a *P*-*T*-*t* sequence; these are shown schematically in Figure
625 12. During the initial blast, the temperature experienced by the desert floor rose to
626 >1500 °C, inducing the decomposition of zircon to tetragonal zirconia and amorphous
627 silica. The rate of cooling was sufficiently rapid to both preserve the zircon cores and
628 prevent the transformation of *α*-quartz to higher temperature quenchable polymorphs.
629 Based on the observation made above, it appears that prior (or possibly coincident
630 with) the onset of the *t* > *m* phase transition, solidification of the bulk glassy material in
631 the surficial 'glassy' Trinitite layer began, resulting in sufficient confining pressure to
632 induce the formation of baddeleyite micro-twins. Initial fallout was likely to have been
633 predominantly molten, owing to the intense heat of the initial fireball and forming
634 mushroom cloud. As the ascending mushroom cloud cools, grains would escape with
635 lesser degrees of melting to be deposited on the solidifying molten surface. Melting of
636 both type-II and type-III quartz grains would continue until the temperature of the glass
637 decreased on the desert floor sufficiently. At the later stages of fallout, no significant
638 thermal alteration would result, and type-I quartz grains would be emplaced at very
639 shallow depths.
640

IMPLICATIONS

In chemically and texturally complex geological samples, the integration of petrographic observations of mineral microstructure and phase relations at all possible scales (centimeter to nanometer) are imperative in deriving the most comprehensive petrologic history possible. The use of advanced sample preparation techniques, such as the focused ion beam microscope, allows an unprecedented precision to sample extraction, while preserving details of original mineral textures down to the near-atomic scale. As the elucidation of mineral processes relies increasingly on developing an atomistic level of understanding, this technique must, ultimately, be more routinely incorporated into petrographic and petrologic studies.

More specifically, in this work, the use of these techniques reveal that textural and compositional evidence preserved by both zircon and quartz may serve to provide some important details pertaining to temperature and pressure conditions present during and immediately subsequent a nuclear explosion. Thus, given their ubiquitous nature in both natural and urban environments (in particular for quartz), analogous nuclear forensic investigations conducted on future PDMs will provide important corroborating evidence in conjunction with the determination of chemical and isotopic fingerprint signatures.

ACKNOWLEDGEMENTS

This work was funded by DOE/NNSA Grant PDP11-40/DE-NA0001112 to A. Simonetti. Partial financial support was also provided by an an NSERC PDF Fellowship awarded to AJL. The authors thank the T. Orlova for assistance with the focused ion beam investigations. We also thank the Notre Dame Energy Materials Characterization

664 Facility for the use of the Jasco micro-Raman spectrometer. We would also like to thank
665 Dr. D. Baker for his editorial assistance as well as Fabrizio Nestola and Lutz Nasdala for
666 their insightful and helpful reviews and comments.

667

668

669 **REFERENCES CITED**

670 Ahearne, J.F., Anspaugh, L.R., Ewing, R.C., Fetter, S.A., Garwin, R.L., Gold, S.P., Grewis,
671 E.G., Hardebeck, T.M., Jeanloz, R., Patterson, W.J., Patton, G.S., Schmitt, H.W., Sevin,
672 E., Tarter, C.B., and Wertheim, R.H. (2005) Effects of Nuclear Earth-Penetrator and
673 Other Weapons. In N.R.C.o.t.N. Academies, Ed, p. 134. The National Academies Press,
674 Washington, D.C.
675 Anseau, M.R., Biloque, J.P., and Fierens, P. (1976) Some studies on thermal solid-state stability
676 of zircon. Journal of Materials Science, 11(3), 578-582.
677 Arora, A.K., Rajalakshmi, M., Ravindran, T.R., and Sivasubramanian, V. (2007) Raman
678 spectroscopy of optical phonon confinement in nanostructured materials. Journal of
679 Raman Spectroscopy, 38(6), 604-617.
680 Bellucci, J.J., and Simonetti, A. (2012) Nuclear forensics: searching for nuclear device debris in
681 trinitite-hosted inclusions. Journal of Radioanalytical and Nuclear Chemistry, 293(1),
682 313-319.
683 Bellucci, J.J., Simonetti, A., Koeman, E.C., Wallace, C., and Burns, P.C. (2014) A detailed
684 geochemical investigation of post-nuclear detonation trinitite glass at high spatial
685 resolution: Delineating anthropogenic vs. natural components. Chemical Geology, 365,
686 69-86.
687 Bellucci, J.J., Simonetti, A., Wallace, C., Koeman, E.C., and Burns, P.C. (2013a) Isotopic
688 Fingerprinting of the World's First Nuclear Device Using Post-Detonation Materials.
689 Analytical Chemistry, 85(8), 4195-4198.
690 Bellucci, J.J., Simonetti, A., Wallace, C., Koeman, E.C., and Burns, P.C. (2013b) Lead Isotopic
691 Composition of Trinitite Melt Glass: Evidence for the Presence of Canadian Industrial
692 Lead in the First Atomic Weapon Test. Analytical Chemistry, 85(15), 7588-7593.

693 Bellucci, J.J., Wallace, C., Koeman, E.C., Simonetti, A., Burns, P.C., Kieser, J., Port, E., and
694 Walczak, T. (2013c) Distribution and behavior of some radionuclides associated with the
695 Trinity nuclear test. Journal of Radioanalytical and Nuclear Chemistry, 295(3), 2049-
696 2057.
697 Bersani, D., Lottici, P.P., and Ding, X.Z. (1998) Phonon confinement effects in the Raman
698 scattering by TiO2 nanocrystals. Applied Physics Letters, 72(1), 73-75.
699 Chen, J.Y., Zheng, H.F., Xiao, W.S., and Zeng, Y.S. (2003) High-temperature and high-
700 pressure cubic zirconia anvil cell for Raman spectroscopy. Applied Spectroscopy,
701 57(10), 1295-1299.
702 Chen, M., Yin, F., Li, X., Xie, X., Xiao, W., and Tan, D. (2013) Natural occurrence of reidite in
703 the Xiuyan crater of China. Meteoritics & Planetary Science, 48(5), 796-805.
704 Cordier, P., and Gratz, A.J. (1995) TEM study of shock metamorphism in quartz from the Sedan
705 nuclear test site. Earth and Planetary Science Letters, 129(1-4), 163-170.
706 Curtis, C.E., and Sowman, H.G. (1953) Investigation of thermal dissociation reassociation and
707 synthesis of zircon. Journal of the American Ceramic Society, 36(6), 190-198.
708 Cygan, R.T., Boslough, M.B., and Kirkpatrick, R.J. (1992) NMR-spectroscopy of experimentally
709 shocked quartz and plagioclase feldspar powders. Proceedings of Lunar and Planetary
710 Science, 22, 127-136.
711 del Monte, F., Larsen, W., and Mackenzie, J.D. (2000) Chemical interactions promoting the
712 ZrO2 tetragonal stabilization in ZrO2-SiO2 binary oxides. Journal of the American
713 Ceramic Society, 83(6), 1506-1512.
714 Donohue, P.H., Simonetti, A., Koeman, E.C., Mana, S., and Burns, P.C. (2015) Nuclear forensic
715 application involving high spatial resolution analysis of Trinitite cross-sections. Journal of
716 Radioanalytical and Nuclear Chemistry.

717 Downs, R.T. (2006) The RRUFF Project: an integrated study of the chemistry, crystallography,
718 Raman and infrared spectroscopy of minerals. 19th General Meeting of the International
719 Mineralogical Association. Kobe, Japan.
720 Eby, G.N., Charnley, N., Pirrie, D., Hermes, R., Smoliga, J., and Rollinson, G. (2015) Trinitite
721 redux: mineralogy and petrology. American Mineralogist, 100, 427-441.
722 Fahey, A.J., Zeissler, C.J., Newbury, D.E., Davis, J., and Lindstrom, R.M. (2010) Postdetonation
723 nuclear debris for attribution. Proceedings of the National Academy of Sciences of the
724 United States of America, 107(47), 20207-20212.
725 Glass, B.P., Liu, S.B., and Leavens, P.B. (2002) Reidite: An impact-produced high-pressure
726 polymorph of zircon found in marine sediments. American Mineralogist, 87(4), 562-565.
727 Goltrant, O., Cordier, P., and Doukhan, J.C. (1991) Planar deformation features in shocked
728 quartz-a transmission electron-microscopy investigation. Earth and Planetary Science
729 Letters, 106(1-4), 103-115.
730 Gouadec, G., and Colomban, P. (2007) Raman Spectroscopy of nanomaterials: How spectra
731 relate to disorder, particle size and mechanical properties. Progress in Crystal Growth
732 and Characterization of Materials, 53(1), 1-56.
733 Gratz, A. (1984) Deformation in laboratory shocked quartz. Journal of Non-Crystalline Solids,
734 67(1-3), 543-558.
735 Grieve, R.A.F., Langenhorst, F., and Stoffler, D. (1996) Shock metamorphism of quartz in
736 nature and experiment .2. Significance in geoscience. Meteoritics & Planetary Science,
737 31(1), 6-35.
738 Gucsik, A., Koeberl, C., Brandstatter, F., Libowitzky, E., and Reimold, W.U. (2004a)
739 Cathodoluminescence, electron microscopy, and Raman spectroscopy of experimentally
740 shock metamorphosed zircon crystals and naturally shocked zircon from the Ries impact
741 crater. 281-322 p.

Gucsik, A., Zhang, M., Koeberl, C., Salje, E.K.H., Redfern, S.A.T., and Pruneda, J.M. (2004b) Infrared and Raman spectra of ZrSiO4 experimentally shocked at high pressures. Mineralogical Magazine, 68(5), 801-811.

Haines, J., Leger, J.M., Hull, S., Petitet, J.P., Pereira, A.S., Perottoni, C.A., and daJornada, J.A.H. (1997) Characterization of the cotunnite-type phases of zirconia and hafnia by neutron diffraction and Raman spectroscopy. Journal of the American Ceramic Society, 80(7), 1910-1914.

Hannink, R.H.J., Kelly, P.M., and Muddle, B.C. (2000) Transformation toughening in zirconia-containing ceramics. Journal of the American Ceramic Society, 83(3), 461-487.

Huffman, A.R., Brown, J.M., Carter, N.L., and Reimold, W.U. (1993) The microstructural response of quartz and feldspar under shock loading at variable temperatures. Journal of Geophysical Research-Solid Earth, 98(B12), 22171-22197.

Hugo, G.R., and Muddle, B.C. (1993) Application of the crystallographic theory to the tetragonal to monoclinic transformation in ceria-zirconia. 665-670 p.

Hugo, G.R., Muddle, B.C., and Hannink, R.H.J. (1988) Crystallography of teh tetragonal to monoclinic transformation in ceria-zirconia. Materials Science Forum, 34-36, 165-169.

Johnson, J.R., Horz, F., and Staid, M.I. (2003) Thermal infrared spectroscopy and modeling of experimentally shocked plagioclase feldspars. American Mineralogist, 88(10), 1575-1582.

Joreau, P., French, B.M., and Doukhan, J.C. (1996) A TEM investigation of shock metamorphism in quartz from the sudbury impact structure (Canada). Earth and Planetary Science Letters, 138(1-4), 137-143.

Kaiser, A., Lobert, M., and Telle, R. (2008) Thermal stability of zircon (ZrSiO4). Journal of the European Ceramic Society, 28(11), 2199-2211.

Knittle, E., and Williams, Q. (1993) High-pressure raman-spectroscopy of zrsio4 - observation of the zircon to scheelite transition at 300-K. American Mineralogist, 78(3-4), 245-252.

768 Koeman, E.C., Simonetti, A., Chen, W., and Burns, P.C. (2013) Oxygen Isotope Composition of
769 Trinitite Postdetonation Materials. Analytical Chemistry, 85(24), 11913-11919.
770 Kowitz, A., Gueldemeister, N., Reimold, W.U., Schmitt, R.T., and Wuennemann, K. (2013a)
771 Diaplectic quartz glass and SiO2 melt experimentally generated at only 5 GPa shock
772 pressure in porous sandstone: Laboratory observations and meso-scale numerical
773 modeling. Earth and Planetary Science Letters, 384, 17-26.
774 Kowitz, A., Schmitt, R.T., Reimold, W.U., and Hornemann, U. (2013b) The first MEMIN shock
775 recovery experiments at low shock pressure (5-12.5 GPa) with dry, porous sandstone.
776 Meteoritics & Planetary Science, 48(1), 99-114.
777 Kumar, P., Saxena, N., Singh, F., and Agarwal, A. (2012) Nanotwinning in CdS quantum dots.
778 Physica B-Condensed Matter, 407(17), 3347-3351.
779 Kusaba, K., Syono, Y., Kikuchi, M., and Fukuoka, K. (1985) Shock behavior of zircon - phase-
780 transition to scheelite structure and decomposition. Earth and Planetary Science Letters,
781 72(4), 433-439.
782 Lambert, P. (1979) Fractures induced by shock in quartz and feldspar. Mineralogical Magazine,
783 43(328), 527-533.
784 Langenhorst, F. (1994) Shock experiments on pre-heated alpha-quartz and beta-quartz .2. X-
785 ray and TEM investigations. Earth and Planetary Science Letters, 128(3-4), 683-698.
786 Langenhorst, F., and Deutsch, A. (1994) Shock experiments on pre-heated alpha-quartz and
787 beta-quartz .1. Optical and density data. Earth and Planetary Science Letters, 125(1-4),
788 407-420.
789 Lenz, C., Nasdala, L., Talla, D., Hauzenberger, C., Seitz, R., and Kolitsch, U. (2015) Laser-
790 induced REE3+ photoluminescence of selected accessory minerals - An "advantageous
791 artefact" in Raman spectroscopy. Chemical Geology, 415, 1-16.

792 Leroux, H., Reimold, W.U., Koeberl, C., Hornemann, U., and Doukhan, J.C. (1999)
793 Experimental shock deformation in zircon: a transmission electron microscopic study.
794 Earth and Planetary Science Letters, 169(3-4), 291-301.
795 McMillan, P.F., Wolf, G.H., and Lambert, P. (1992) A raman-spectroscopic study of shocked
796 single crystalline quartz. Physics and Chemistry of Minerals, 19(2), 71-79.
797 Muddle, B.C., and Hannink, R.H.J. (1986) Crystallography of the tetragonal to monoclinic
798 transformation in mgo-partially-stabilized zirconia. Journal of the American Ceramic
799 Society, 69(7), 547-555.
800 Nakano, Y., Goto, K., Matsui, T., Tada, R., and Tajika, E. (2008) PDF orientations in shocked
801 quartz grains around the Chicxulub crater. Meteoritics & Planetary Science, 43(4), 745-
802 760.
803 Ostertag, R. (1983) Shock experiments on feldspar crystals. Journal of Geophysical Research,
804 88, B364-B376.
805 Parekh, P.P., Semkow, T.M., Torres, M.A., Haines, D.K., Cooper, J.M., Rosenberg, P.M., and
806 Kitto, M.E. (2006) Radioactivity in Trinitite six decades later. Journal of Environmental
807 Radioactivity, 85(1), 103-120.
808 Pavlik, R.S., Holland, H.J., and Payzant, E.A. (2001) Thermal decomposition of zircon
809 refractories. Journal of the American Ceramic Society, 84(12), 2930-2936.
810 Piazolo, S., Austrheim, H., and Whitehouse, M. (2012) Brittle-ductile microfabrics in naturally
811 deformed zircon: Deformation mechanisms and consequences for U-Pb dating.
812 American Mineralogist, 97(10), 1544-1563.
813 Pidgeon, R.T., Nemchin, A.A., and Kamo, S.L. (2011) Comparison of structures in zircons from
814 lunar and terrestrial impactites. Canadian Journal of Earth Sciences, 48(2), 107-116.
815 Ravindran, T.R., and Yadav, K. (2015) Re-examination of high pressure orthorhombic-I phase
816 of ZrO2 by Raman spectroscopy. The European Physical Journal B, 88(1), 1434-6036.

Reimold, W.U., Leroux, H., and Gibson, R.L. (2002) Shocked and thermally metamorphosed zircon from the Vredefort impact structure, South Africa: a transmission electron microscopic study. European Journal of Mineralogy, 14(5), 859-868.

Rhodes, R. (1986) The making of the atomic bomb. Simon & Schuster, New York.

Ross, C.S. (1948) Optical properties of glass from Alamogordo, New-Mexico. American Mineralogist, 33(5-6), 360-362.

Schmieder, M., Reimold, W.U., Buchner, E., Khirfan, M., Salameh, E., and Khoury, H. (2011) Shock-metamorphic microfeatures in chert from the Jebel Waqf as Suwwan impact structure, Jordan. Meteoritics & Planetary Science, 46(4), 574-586.

Staritzky, E. (1950) Thermal effects of atomic bomb explosions on soils at Trinitiy and Eniwetok. In L.A.S. Lab, Ed, 21, p. 1-21.

Stoffler, D. (1971) Progressive metamorphism and classification of shocked and brecciated crystalline rocks at impact craters. Journal of Geophysical Research, 76(23), 5541-&.

Stoffler, D., and Langenhorst, F. (1994) Shock metamorphism of quartz in nature and experiment .1. Basic observation and theory. Meteoritics, 29(2), 155-181.

Timms, N.E., Erickson, T.M., Schmieder, M., Tohver, E., and Pearce, M. (2014) Shock Recrystallisation and Decomposition of Zircon. Meteoritics & Planetary Science, 49, A397-A397.

Trepmann, C.A. (2008) Shock effects in quartz: Compression versus shear deformation - An example from the Rochechouart impact structure, France. Earth and Planetary Science Letters, 267(1-2), 322-332.

Trepmann, C.A., and Spray, J.G. (2006) Shock-induced crystal-plastic deformation and post-shock annealing of quartz: microstructural evidence from crystalline target rocks of the Charlevoix impact structure, Canada. European Journal of Mineralogy, 18(2), 161-173.

Turner, D., Langenhorst, F., and Pollok, K. (2014) Martensitic mechanism of the zircon-to-reidite transformation. Meteoritics & Planetary Science, 49, A406-A406.

Wallace, C., Bellucci, J.J., Simonetti, A., Hainley, T., Koeman, E.C., and Burns, P.C. (2013) A multi-method approach for determination of radionuclide distribution in trinitite. Journal of Radioanalytical and Nuclear Chemistry, 298(2), 993-1003.

Wittmann, A., Kenkmann, T., Schmitt, R.T., and Stoffler, D. (2006) Shock-metamorphosed zircon in terrestrial impact craters. Meteoritics & Planetary Science, 41(3), 433-454.

Zanetti, M., Wittmann, A., Nemchin, A., Carpenter, P., Vicenzi, E.P., and Jolliff, B. (2014) Decomposition of zircon in mistastin lake impact melt glass: an integrated sims, hyperspectral-cl, raman and EPMA study. Meteoritics & Planetary Science, 49, A449-A449.

852 **LIST OF FIGURES & CAPTIONS**

853

854 **FIGURE 1.** A selection of altered zircon grains from various Trinitite petrographic thin
855 sections: (a-b) 5b 1022a (glassy section); (c) 5a 606b (glassy section); 5a 606b
856 (sandy section); (e) TS1 (glassy section); (f) 3525b (glassy section); and (g-h)
857 TS1 (glassy section). The red box and blue line in (g) indicate the region of the
858 [2]-dimensional Raman spectra shown in Figure 2*c*,*d* and the orientation of TEM
859 foil prepared by FIB, respectively.

860

861 **FIGURE 2.** Raman spectra (532 nm) of Trinitite zircon grains. Typical spectra from
862 zircons in Figure 1 corresponding to (a) core and (b) fibrous regions. (c) and (d)
863 show [2] -dimensional Raman maps plotting the intensity variation of band
864 centered at 1009 cm^{-1} and 590 cm^{-1}, respectively, for the zircon grain show in
865 Figure 1g-h: c, f, and g (as well as dotted red lines) delineate core, fibrous, and
866 glassy regions, respectively, as defined in the SEM image. A comparison of band
867 positions in the 400-650 cm^{-1} of the observed, edge-region spectrum (*e*) and a
868 baddeleyite reference taken from the online RRUFF database (specimen
869 R060078) (*f*). The colored dashed lines highlight the relative shifts to higher
870 vibrational energies.

871

872 **FIGURE 3.** Transmission electron microscope to zircon foil (Zr09). (*a*-*g*) images in
873 bright field mode; (h) schematic trace of (a) highlighting the orientation of fiber
874 axes (green lines) relative to twin planes (purple dotted line).

875

876 **FIGURE 4.** Variation in Si, Zr, and O along traverse on Zr09. The corresponding
877 phase identities have been inset. X-ray fluorescence spectra taken with TEM
878 operating in STEM mode. Intensity variation corresponds to band intensities for
879 Zr (L*α*, 2.04 keV), Si (K*α*, 1.74 kEv), and O (K*α*, 0.53 keV).

880

881 **FIGURE 5.** TEM image compilation image of fiber cross-section shown in (a) (see
882 also, blue circle in Figure 2). (c-d) are HRTEM images of various twin variants.
883 The image clearly shows the continuity of twin planes throughout the fibers and
884 the three structural orientations, as indicated by the orientations of the colored
885 arrow.

886

887 **FIGURE 6.** Diffraction pattern of baddeleyite twin. (a) the SAED pattern collected on
888 the fiber shown in Figure 7. (b-d) Fourier transform calculated diffraction patterns
889 of each twin variant; outline colors coincide with arrows in Figure 8; (e)
890 summation of individual patters shows recreates the pattern in (a); (f) illustrates
891 the indexed patterns for each of the three lattices, viewed down zone axis [010]
892 (blue spots), [0-10] (red spots), and [100] (greed spots); and (g) illustrates
893 relative axial orientations of the three color-coded twin variants; the relative
894 orientations are consistent in (e) through (g). The (*) adjacent to reflections spots
895 indicates those that are present but should be systematically absent.

896

FIGURE 7. Optical microscope images of quartz grains taken in plane-polarized (left column) and cross-polarized (right column) light. Type-I grains from sandy regions of 5a 886b (*a*,*b*) and 5b 10.22a (*c*,*d*); Type-II grains from glassy region of 5a 886b (*e*,*f*); Type-III grains from glassy region of 5a 886b (*g*,*h*). The dotted pink outlines show the individual grains; the straight dotted orange lines indicate the approximate location and orientation of the TEM foil prepared by FIB. Scale of all images are as indicated in (*a*).

FIGURE 8. Images of a type-II grain from Trinitite section 5b 10.22a. (a) in plane-polarized light at low magnification and (b) at higher magnification; (c) in cross-polarized light showing the mottled extinction texture; (d) SEM image taken in backscatter mode showing the fragmentation of crystalline quartz in the glass matrix.

FIGURE 9. TEM images of quartz grains imaged in Figure 7. (*a*-*b*) highlights the thermal decomposition of early stage the type-II quartz grain from section TS1 imaged in Figure 7g-h; (c-d) show bright-field and dark-field images highlighting the advanced thermal progressive vitrification of quartz type-II grains from section 5b 10.22a imaged in Figure 7*e*-*f*. Both images (e) and (f) show micrographs of the type-I grains in Figure 7c,d indicated by the red and blue arrow, respectively.

FIGURE 10. Alpha-track radiographs (right column) compared with distribution of quartz types (left column) in four selected Trinitite thin sections cut (approximately) vertically to the desert surface: (*a*,*b*) TS1; (*c*,*d*) 5A 8.86B; (*e*,*f*) 4C 8.56B; and (*g*,*h*) 4F 5.37A. Quartz grains are colored as follows: type-I (pink), type-II (green), and type-III (orange). The purple arrow indicates 'way-up', as determined by alpha-track distribution.

FIGURE 11. Pressure-temperature diagram shows the approximate distribution of significant zirconia phases as well as the typical *P*-*T* variation associated with impact events (Wittman et al. 2006) and the shock stages of Stoffler (1971). The dimensions of the purple box represents the maximum *P* and *T* conditions indicated by the analyses of quartz and zircon grains. *Note*: the superimposed zirconia phase diagram is meant mostly as a guide, as the abscissa should rightly be labeled as simply '*pressure*' and not shock pressure.

FIGURE 12. Schematic showing relative timing of events leading to the creation of Trinitite PDM immediately following the detonation of "*The Gadget*" during the Trinity test.

937

938

This is a preprint, the final version is subject to change, of the American Mineralogist (MSA)
Cite as Authors (Year) Title. American Mineralogist, in press.
(DOI will not work until issue is live.) DOI: http://dx.doi.org/10.2138/am-2017-5739

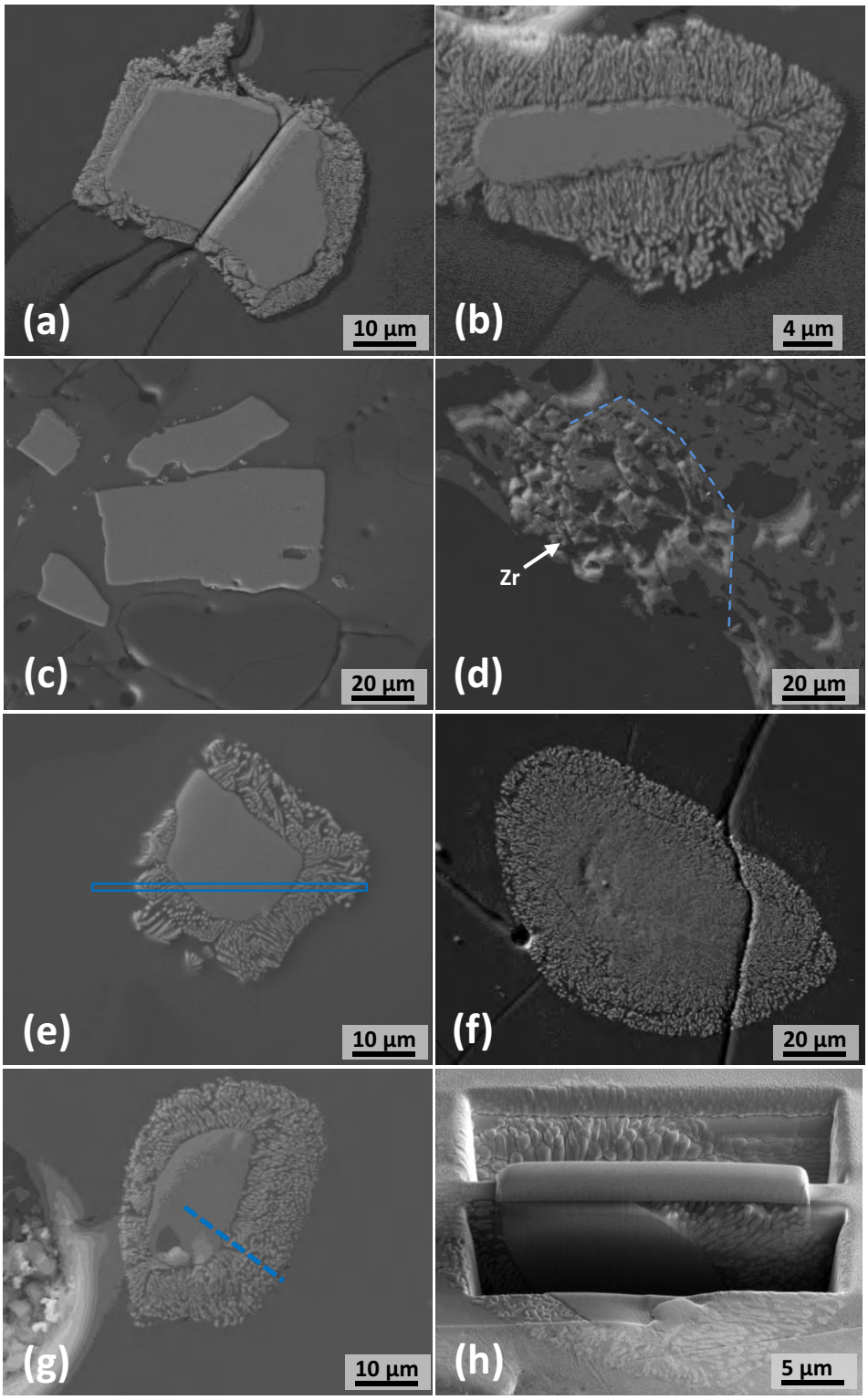

FIGURE 1

This is a preprint, the final version is subject to change, of the American Mineralogist (MSA)
Cite as Authors (Year) Title. American Mineralogist, in press.
(DOI will not work until issue is live.) DOI: http://dx.doi.org/10.2138/am-2017-5739

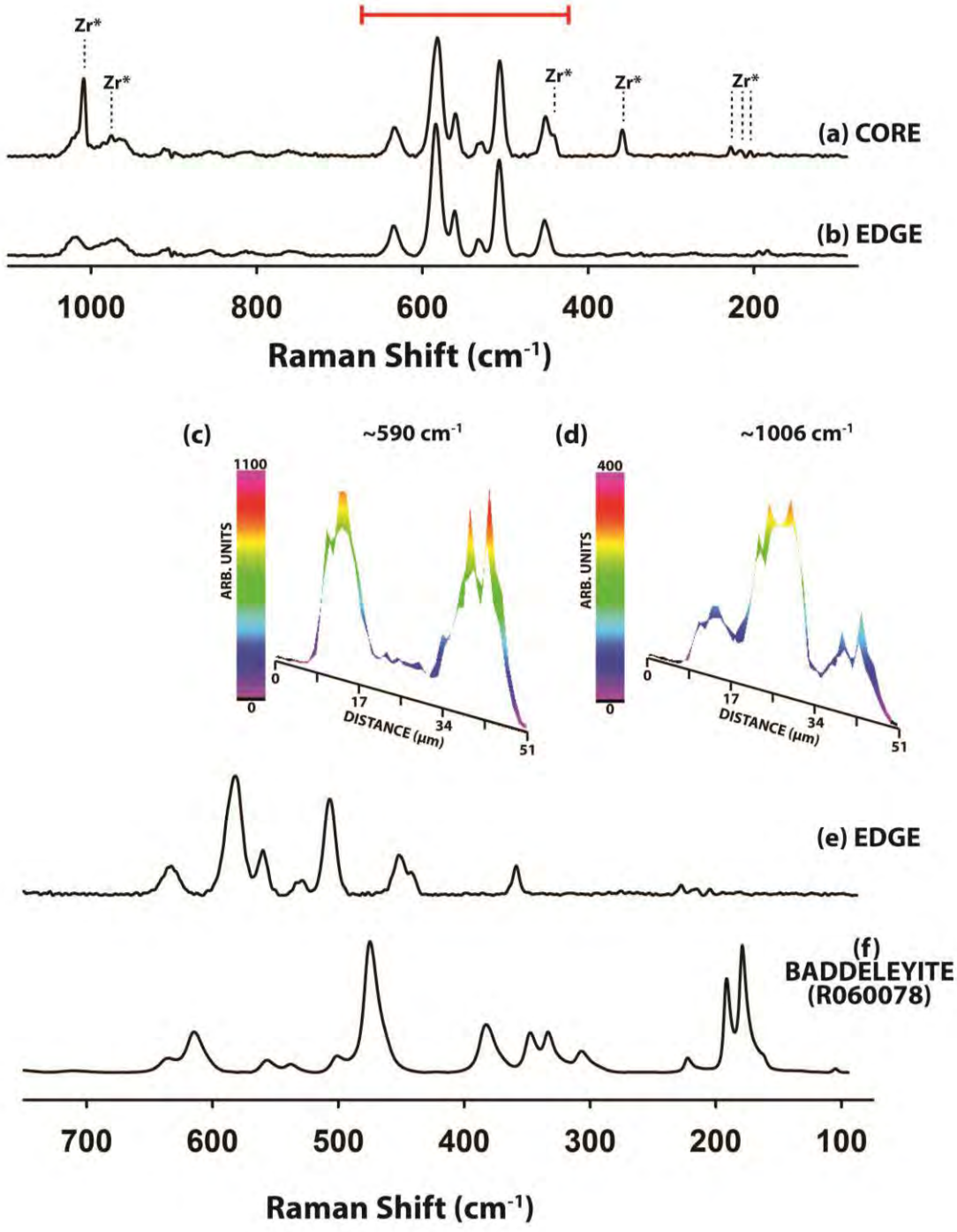

FIGURE 2

This is a preprint, the final version is subject to change, of the American Mineralogist (MSA)
Cite as Authors (Year) Title. American Mineralogist, in press.
(DOI will not work until issue is live.) DOI: http://dx.doi.org/10.2138/am-2017-5739

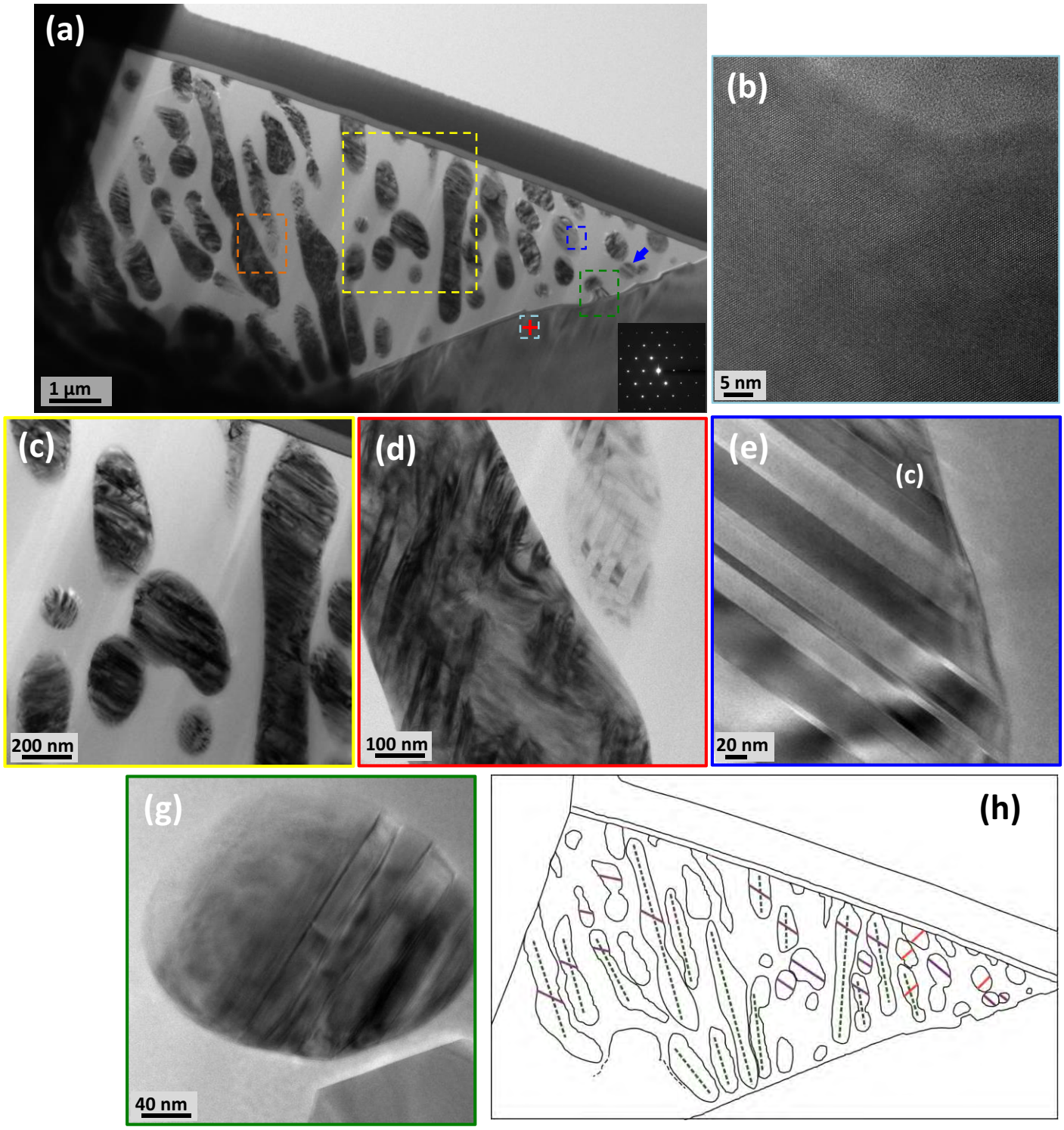

FIGURE 3

This is a preprint, the final version is subject to change, of the American Mineralogist (MSA)
Cite as Authors (Year) Title. American Mineralogist, in press.
(DOI will not work until issue is live.) DOI: http://dx.doi.org/10.2138/am-2017-5739

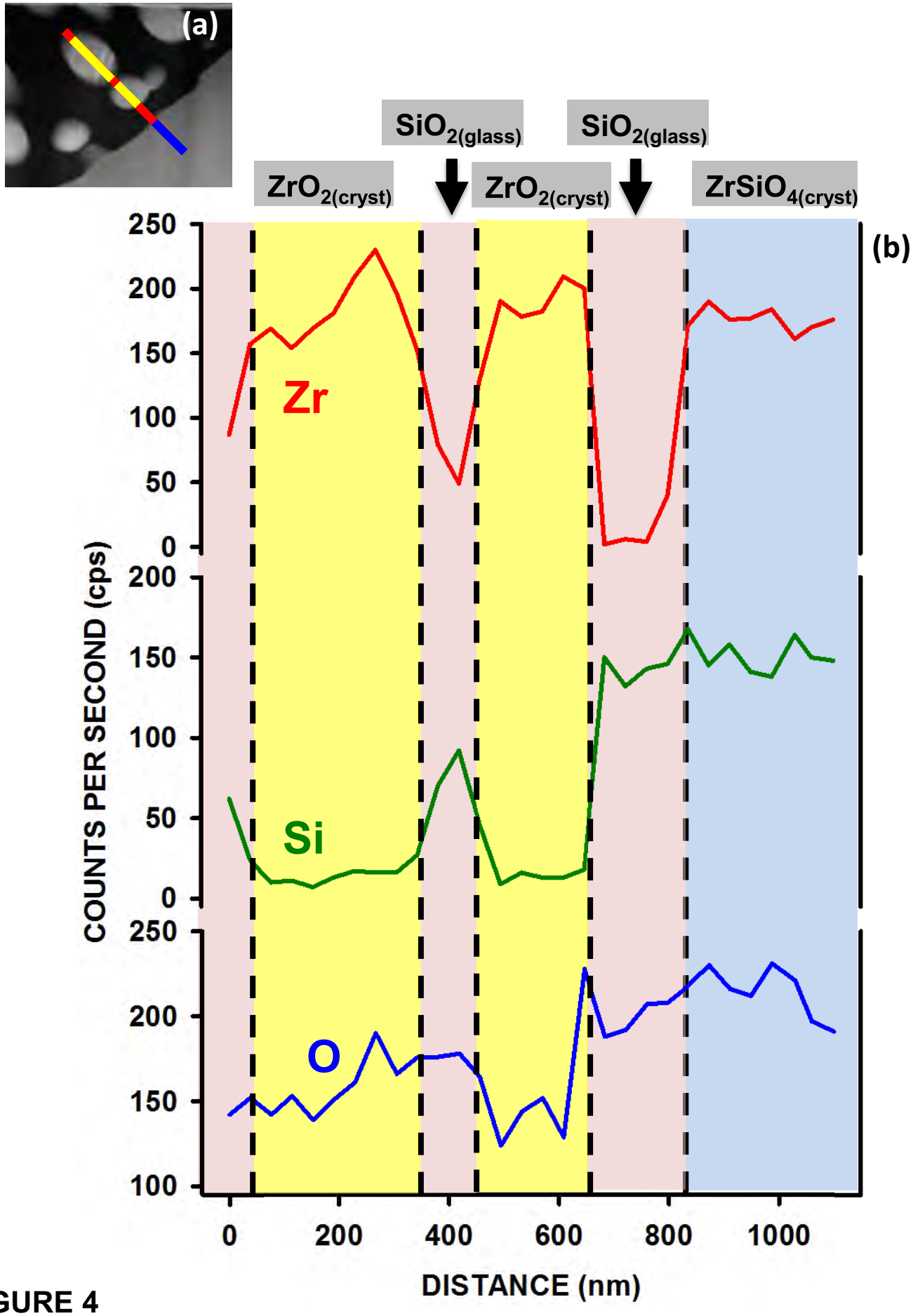

FIGURE 4

This is a preprint, the final version is subject to change, of the American Mineralogist (MSA)
Cite as Authors (Year) Title. American Mineralogist, in press.
(DOI will not work until issue is live.) DOI: http://dx.doi.org/10.2138/am-2017-5739

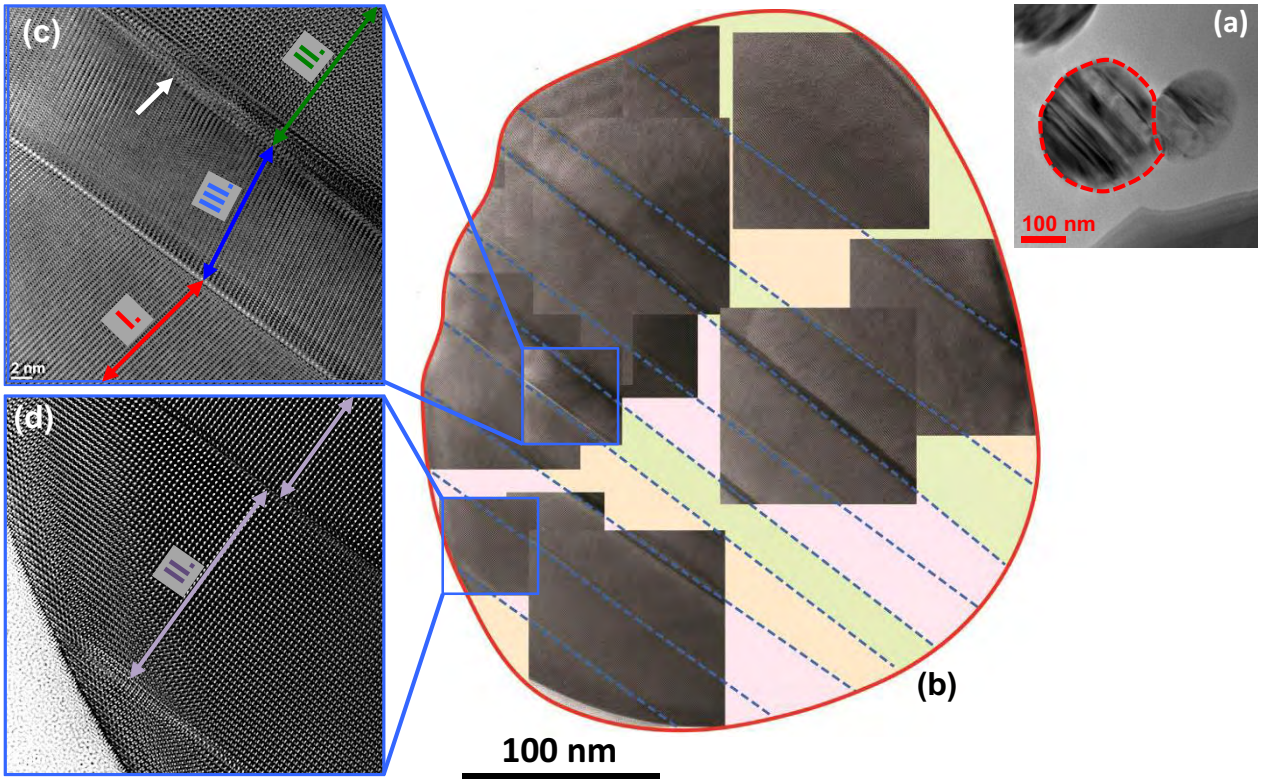

FIGURE 5

This is a preprint, the final version is subject to change, of the American Mineralogist (MSA)
Cite as Authors (Year) Title. American Mineralogist, in press.
(DOI will not work until issue is live.) DOI: http://dx.doi.org/10.2138/am-2017-5739

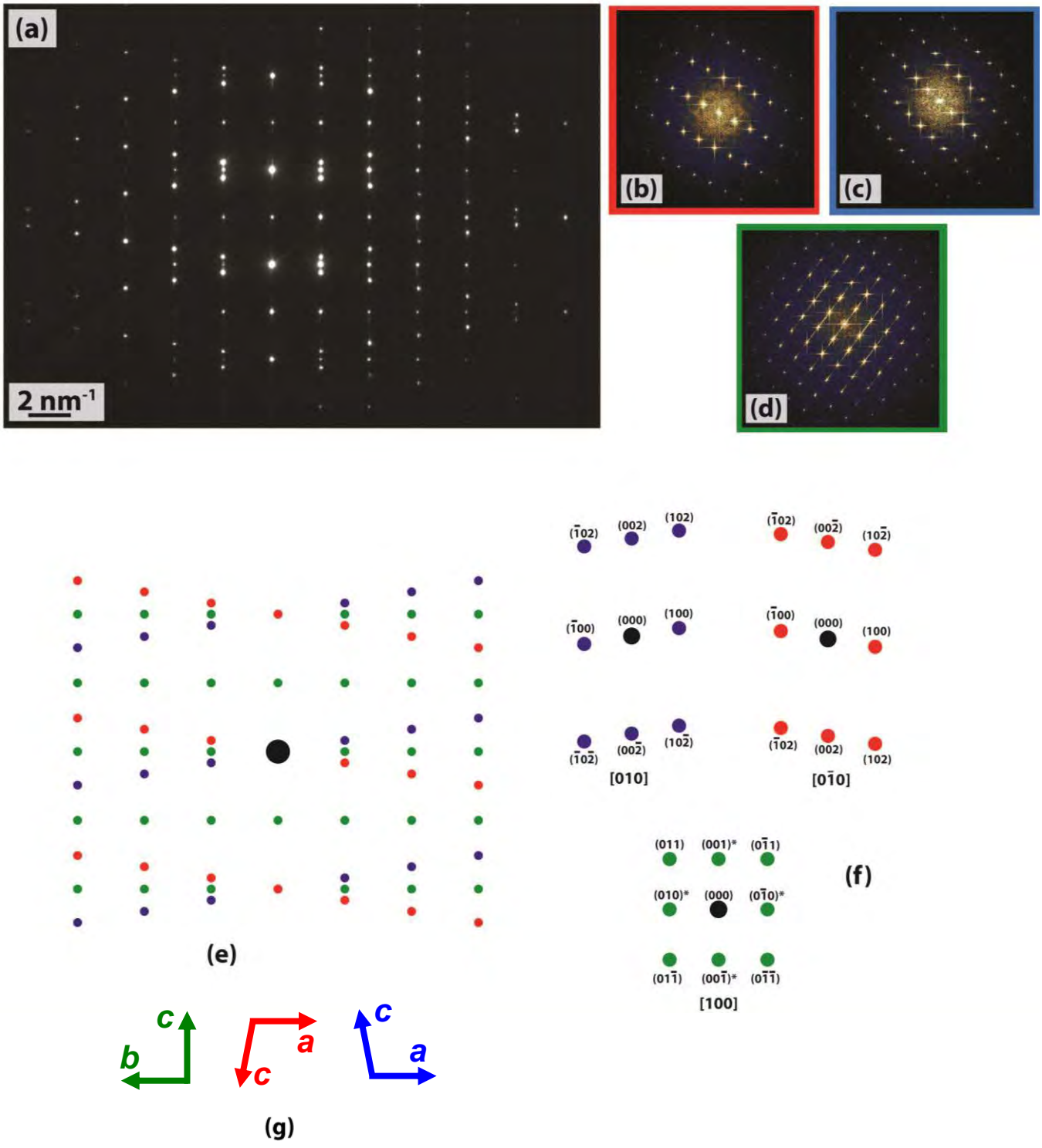

FIGURE 6

This is a preprint, the final version is subject to change, of the American Mineralogist (MSA)
Cite as Authors (Year) Title. American Mineralogist, in press.
(DOI will not work until issue is live.) DOI: http://dx.doi.org/10.2138/am-2017-5739

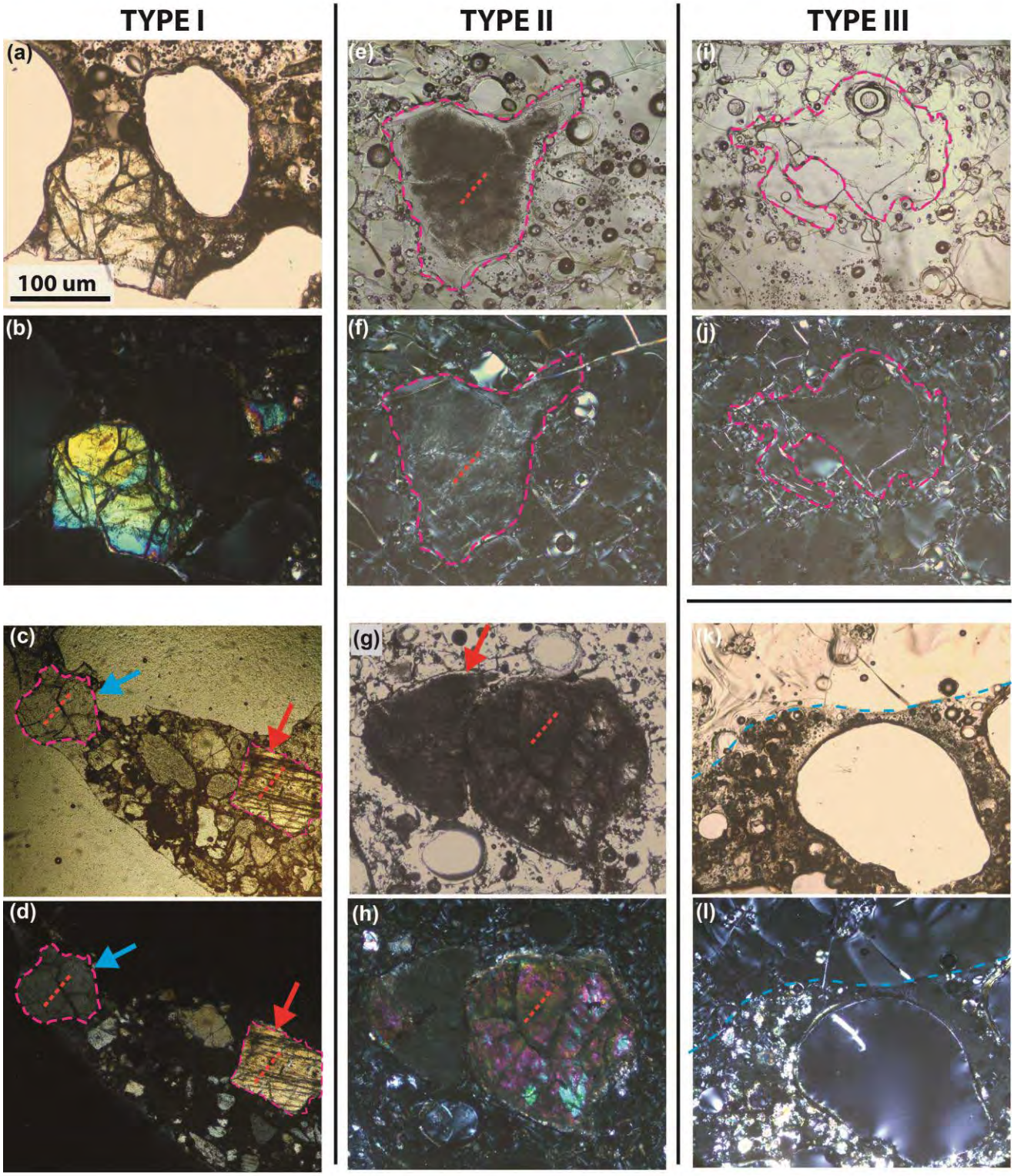

FIGURE 7

This is a preprint, the final version is subject to change, of the American Mineralogist (MSA)
Cite as Authors (Year) Title. American Mineralogist, in press.
(DOI will not work until issue is live.) DOI: http://dx.doi.org/10.2138/am-2017-5739

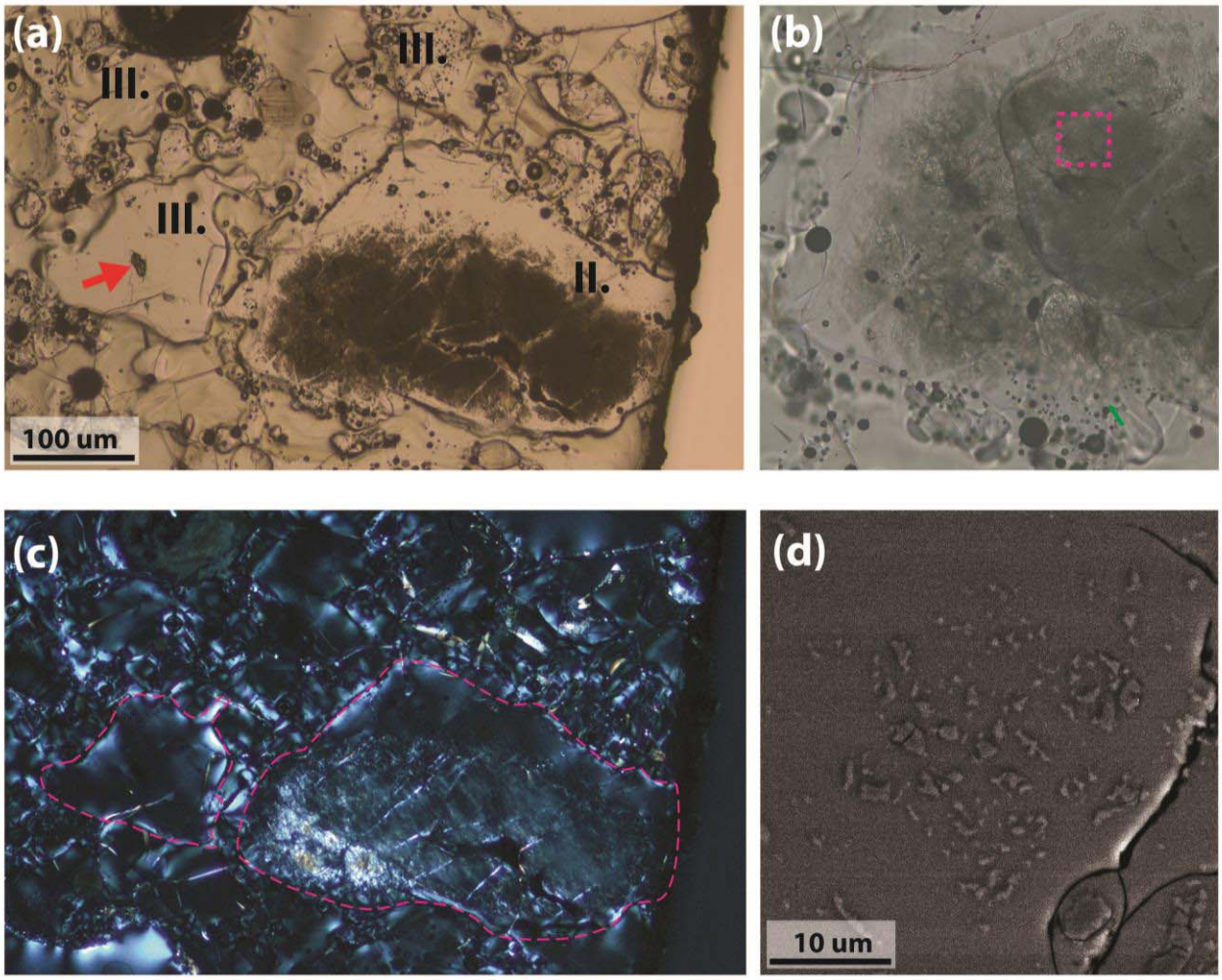

FIGURE 8

This is a preprint, the final version is subject to change, of the American Mineralogist (MSA)
Cite as Authors (Year) Title. American Mineralogist, in press.
(DOI will not work until issue is live.) DOI: http://dx.doi.org/10.2138/am-2017-5739

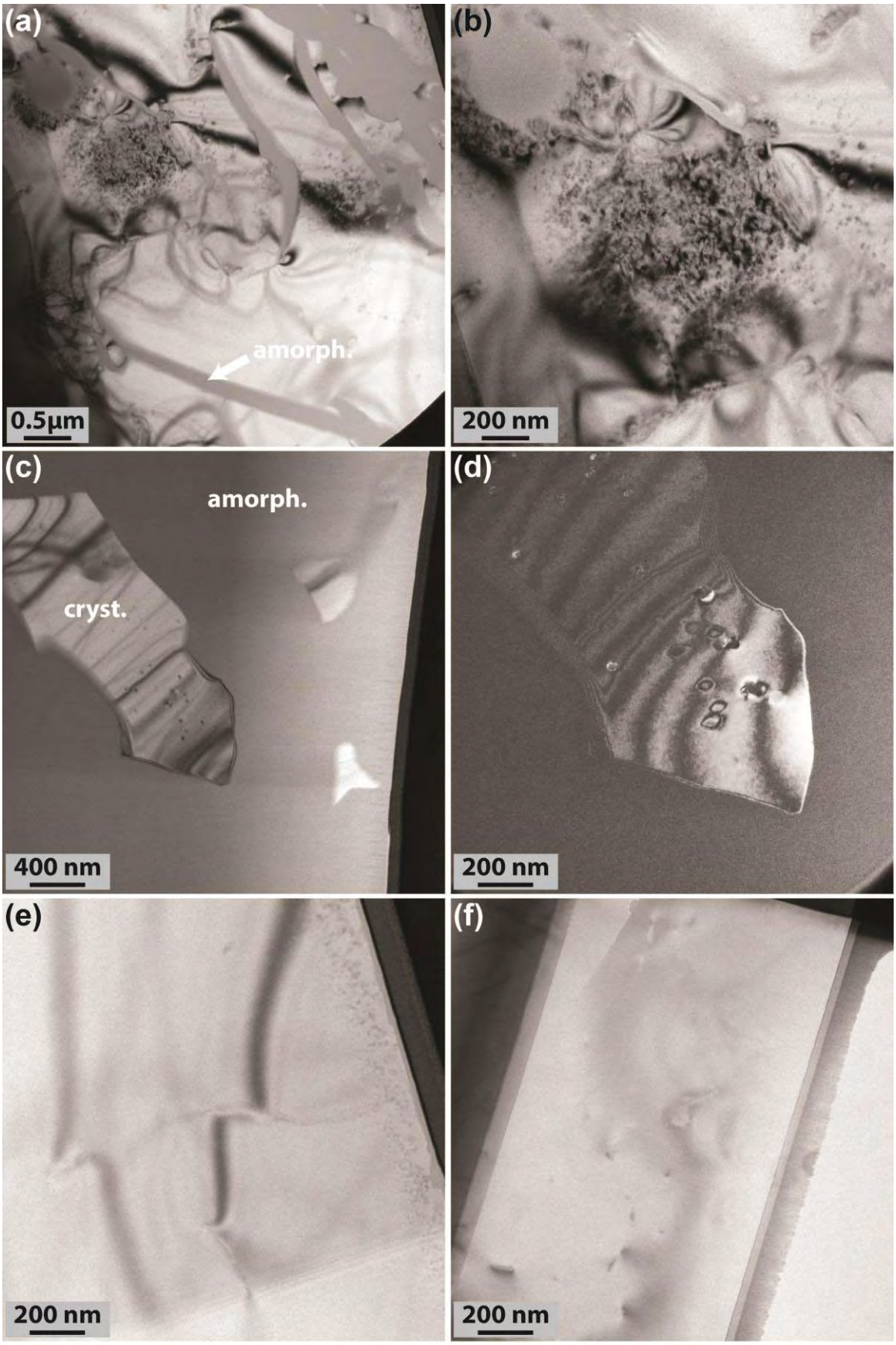

FIGURE 9

This is a preprint, the final version is subject to change, of the American Mineralogist (MSA)
Cite as Authors (Year) Title. American Mineralogist, in press.
(DOI will not work until issue is live.) DOI: http://dx.doi.org/10.2138/am-2017-5739

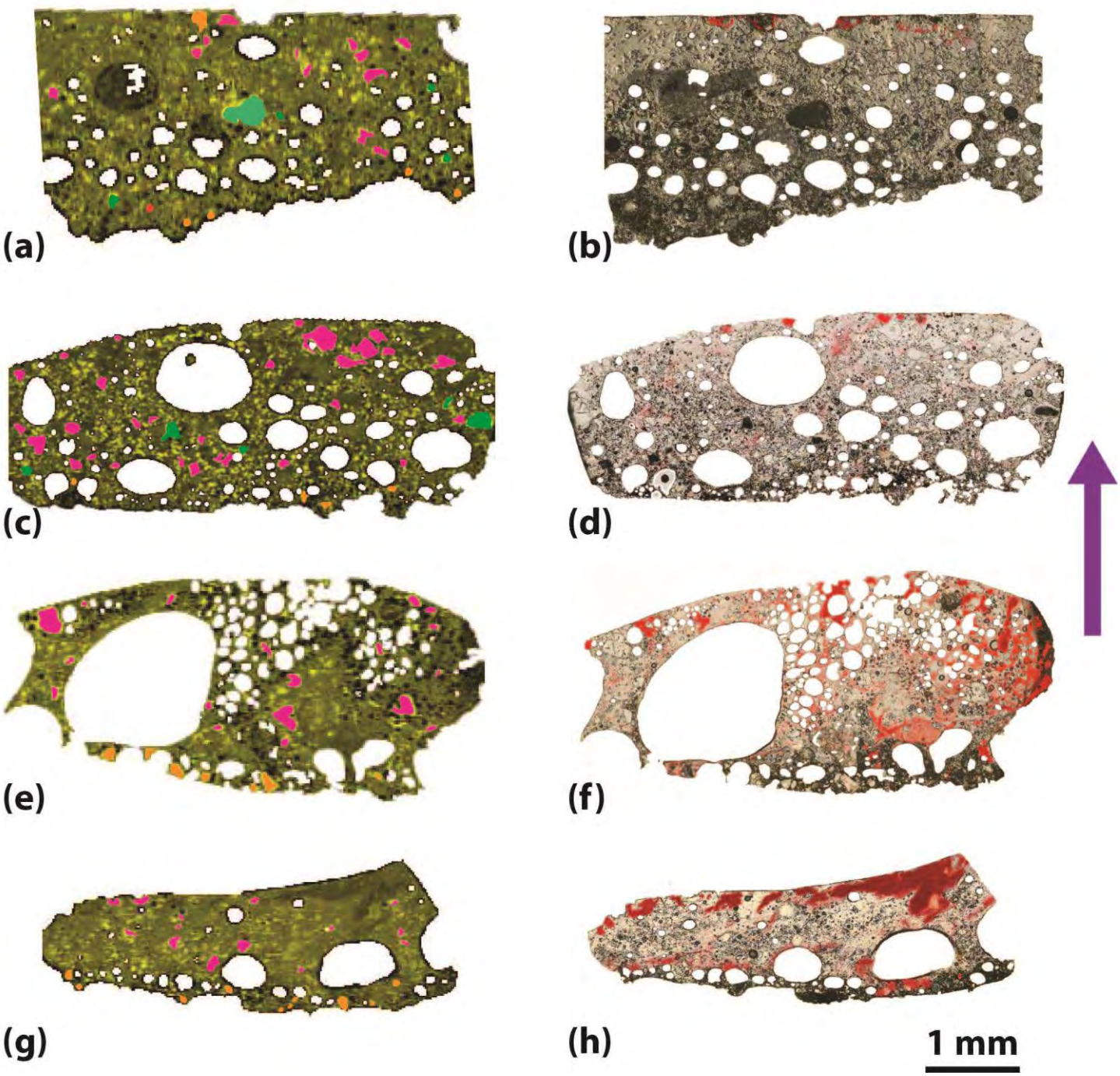

FIGURE 10

This is a preprint, the final version is subject to change, of the American Mineralogist (MSA)
Cite as Authors (Year) Title. American Mineralogist, in press.
(DOI will not work until issue is live.) DOI: http://dx.doi.org/10.2138/am-2017-5739

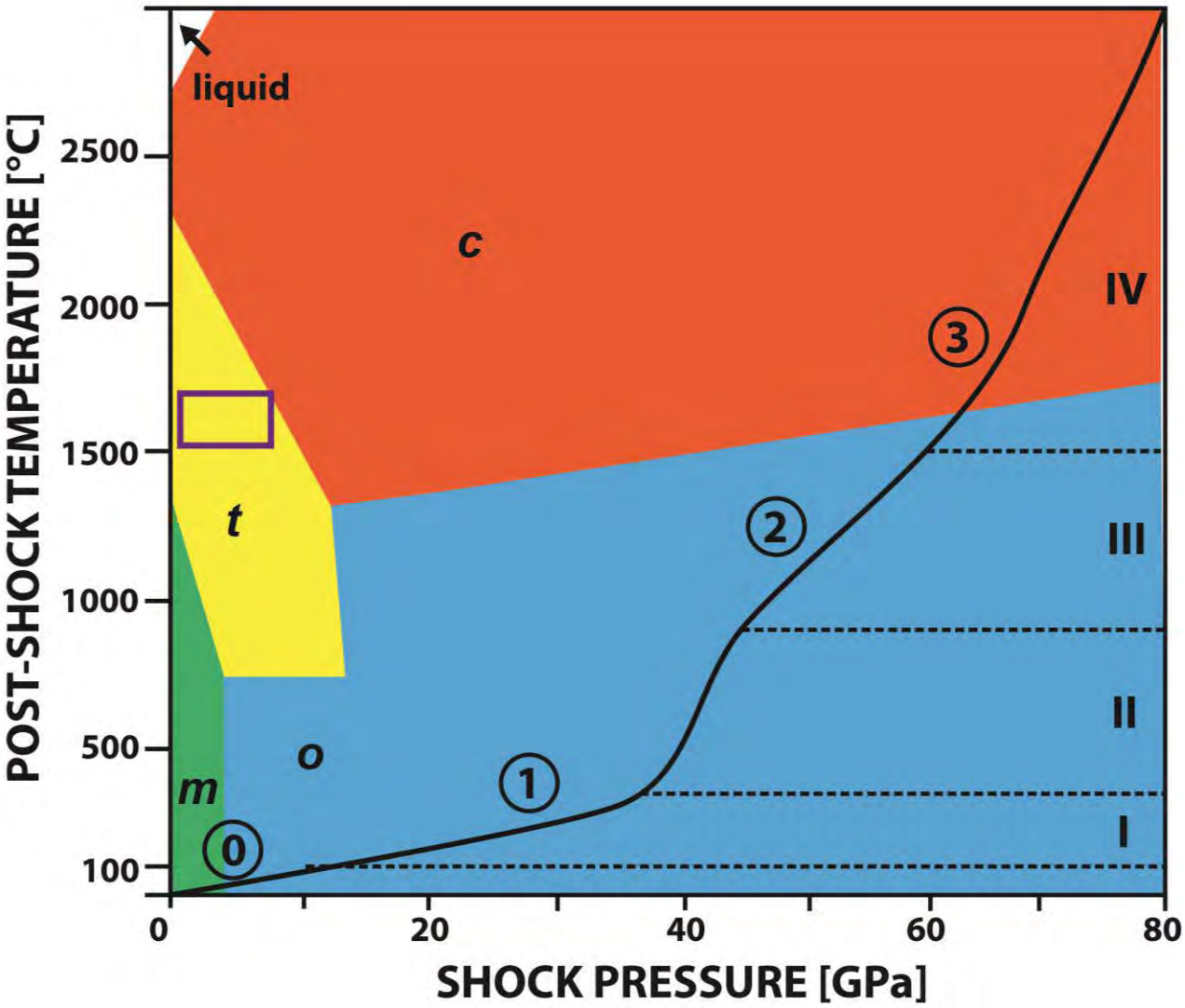

FIGURE 11

This is a preprint, the final version is subject to change, of the American Mineralogist (MSA)
Cite as Authors (Year) Title. American Mineralogist, in press.
(DOI will not work until issue is live.) DOI: http://dx.doi.org/10.2138/am-2017-5739

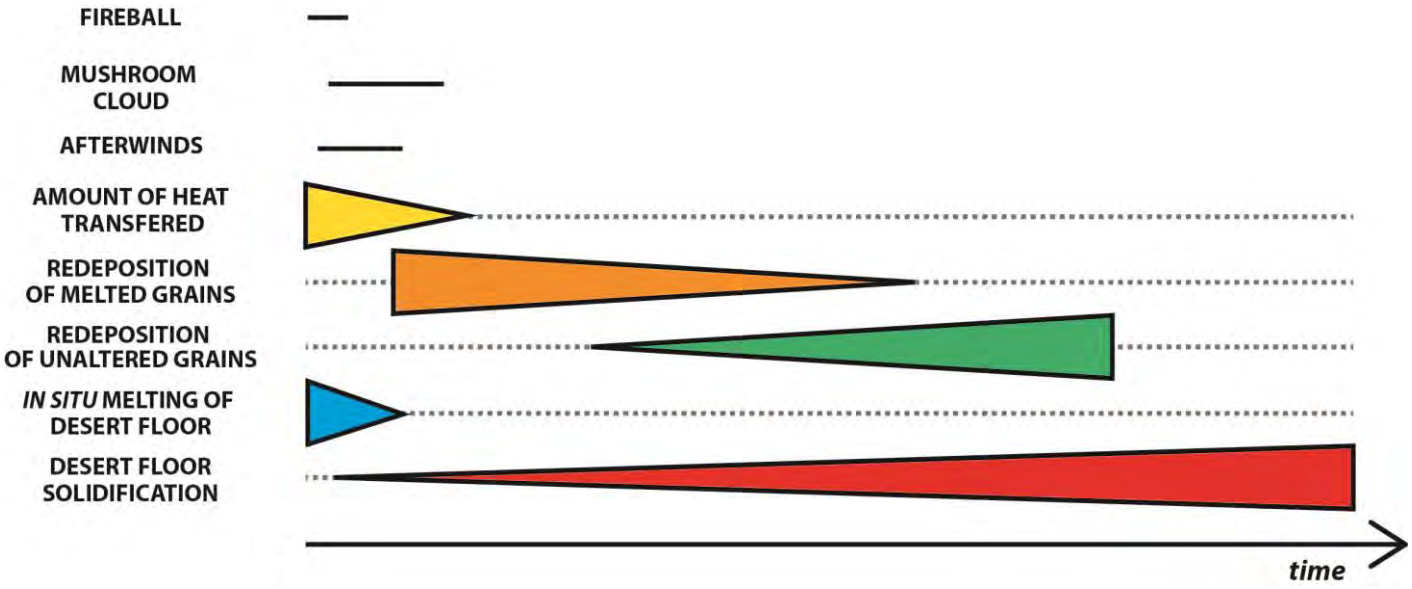

FIGURE 12